Eur. Phys. J. B (2024)97:173
https://doi.org/10.1140/epjb/s10051-024-00805-1

THE EUROPEAN PHYSICAL JOURNAL B

Regular Article - Solid State and Materials

Unveiling the structural, electronic, optical, mechanical, and thermodynamic properties of Mg_3ZnO_4 in a Caswellsilverite-like structure: a DFT study

Moufdi Hadjab[1,2,a], Mohamed Issam Ziane[3], Abderrahim Hadj Larbi[4], Hamza Bennacer[1,5], Mehrdad Faraji[6,7], and Olga Guskova[2,8]

[1] Department of Electronics, Faculty of Technology, University of M'sila, University Pole, Road Bourdj Bou Arreridj, 28000 M'sila, Algeria
[2] Institute of Theory of Polymers, Leibniz Institute of Polymer Research Dresden, 01069 Dresden, Germany
[3] Laboratory of Electrical and Materials Engineering (LGEM), Higher School of Electrical and Energetic Engineering of Oran (ESGEEO), Oran, Algeria
[4] Research Center in Industrial Technologies CRTI, Cheraga, P. O. Box 64, 16014 Algiers, Algeria
[5] Elaboration and Physico-Mechanical and Metallurgical Characterization of Materials Laboratory, ECP3M, University of Mostaganem, Mostaganem, Algeria
[6] Istituto Italiano di Tecnologia, Via Morego 30, 16163 Genoa, Italy
[7] Dipartimento di Chimica e Chimica Industriale, Università degli Studi di Genova, Via Dodecaneso 31, 16146 Genoa, Italy
[8] Dresden Center for Computational Materials Science (DCMS), Technische Universität Dresden, 01062 Dresden, Germany

Received 9 September 2024 / Accepted 11 October 2024

Abstract. This study investigates the physical properties of the novel mixed metal oxide Mg_3ZnO_4, emphasizing its potential in optoelectronic manufacturing. We provide a comprehensive analysis of its structural, optoelectronic, mechanical, and thermodynamic characteristics, focusing on the ternary compound, which crystallizes in a rocksalt phase similar to the mineral Caswellsilverite. Using advanced density functional theory (DFT) and the Full-Potential Linearized Augmented Plane Wave (FP-LAPW) method within the WIEN2k package, we predict the material's properties in detail. Our structural analysis confirms the stability of Mg_3ZnO_4 in the cubic $Pm\bar{3}m$ space group, revealing key crystallographic parameters. The electronic structure calculations indicate a well-defined energy band gap, confirming its semiconducting nature and suitability for optoelectronic applications. Optical properties, including the dielectric function, absorption, and reflection spectra, demonstrate significant light interaction, highlighting the material's potential for UV photodetectors and photovoltaic solar cells. The investigation of elastic properties provides critical insights into the mechanical strength and durability of Mg_3ZnO_4, further supporting its viability for demanding applications. Additionally, our thermodynamic analysis reveals the material's behavior under varying environmental conditions, reinforcing its potential in high-performance optoelectronic devices. These findings establish Mg_3ZnO_4 as a promising candidate for advanced thin-film solar cells and pave the way for future experimental and theoretical studies to explore its unique properties for innovative technological applications.

1 Introduction

Metal oxide semiconductors are regarded as promising advanced functional materials due to their chemical stability, wide band gap, and low cost [1, 2]. Among these oxides, the magnesium zinc oxide (MgZnO) alloy has emerged as a highly promising material in semiconductor research due to its exceptional optical properties, particularly in the ultraviolet (UV) photonics spectrum [3, 4]. This alloy not only demonstrates superior optical performance but also features an environmentally benign chemical profile. Such characteristics position $Mg_xZn_{1-x}O$ as a critical material for the next generation of semiconductor devices, where there is an increasing demand for materials that offer both high performance and environmental sustainability. The dual benefits of $Mg_xZn_{1-x}O$—its superior optical properties and eco-friendly nature—make it highly relevant in a range of applications, spanning both technological innovation and environmental stewardship [5].

[a] e-mail: moufdi.hadjab@univ-msila.dz (corresponding author)

Published online: 07 November 2024

As a member of the transparent conductive oxides (TCOs) family, $Mg_xZn_{1-x}O$ has captured considerable attention for its potential use in a broad spectrum of optoelectronic devices [6, 7]. These include ultra-thin-film solar cells, which benefit from the material's excellent transparency and conductivity [8], violet light-emitting diodes (LEDs) [9], and high-voltage transparent thin-film transistors (HVTTFT) [10]. The ability of $Mg_xZn_{1-x}O$ to function as a transparent conductive electrode [11, 12] is particularly noteworthy, as it underscores the material's versatility in applications that require both high electrical conductivity and optical transparency. Additionally, $Mg_xZn_{1-x}O$ has shown significant promise in the progress of ultra-high response solar-blind UV detectors, where its optical properties are leveraged to detect UV light while remaining insensitive to visible light [13].

Despite the significant advances made in the development of $Mg_xZn_{1-x}O$-based technologies, challenges remain in identifying stable and efficient Mg–Zn–O systems under ambient conditions. One of the primary objectives of this research is to predict and analyze such systems using the first-principles methods. The rocksalt structure of the $Mg_xZn_{1-x}O$ alloy has been a focal point in both theoretical and experimental studies. Notable theoretical works by Amrani et al. [14] and Aoumeur et al. [15] utilized the Full-Potential Linear-Muffin-Tin-Orbital (FP-LMTO) technique [16] to investigate the electronic, structural, and thermodynamic characteristics of $Mg_xZn_{1-x}O$ across various concentrations. These studies employed several density functional theory (DFT) approximations, including the Local Density Approximation (LDA) [17], the Perdew–Burke–Ernzerhof Generalized Gradient Approximation (PBE-GGA) [18] and its enhanced form, and the Engel–Vosko GGA (EV-GGA) [19], to provide comprehensive insights into the material's behavior across different compositions.

Further investigations by Drissi [20] and Hadjab [21] extended the focus to the optoelectronic properties of $Mg_xZn_{1-x}O$, using the Full-Potential Linearized Augmented Plane Wave (FP-LAPW) method with various exchange–correlation functionals, such as LDA [17], the Wu-Cohen GGA (WC-GGA) [22], and the more recently advanced Tran–Blaha modified semi-local Becke–Johnson potential (TB-mBJ) [23]. These studies highlight the significance of $Mg_xZn_{1-x}O$'s electronic and optical properties, emphasizing its potential for optoelectronic applications.

On the experimental front, research has primarily concentrated on the growth and characterization of $Mg_xZn_{1-x}O$ films, with early efforts successfully achieving MgO compositions up to 33 mol% through non-equilibrium growth techniques [24–26]. The majority of these studies focused on $Mg_xZn_{1-x}O$/ZnO superlattices or layers, examining their optoelectronic properties under varying growth conditions [27, 28]. More recently, there has been an increasing interest in synthesizing epitaxial layers of $Mg_xZn_{1-x}O$ with a rocksalt structure. Pioneering investigations by Tian et al. [29], Kaneko et al. [30], and Dłuzewski et al. [31] have demonstrated the feasibility of growing these structures, albeit with challenges in achieving rocksalt configurations for compositions with $x > 0.5$. One of the few successes in this area was reported by Kaneko et al. [30], who employed the mist chemical vapor deposition (CVD) method to grow $Mg_xZn_{1-x}O$ ($x > 0.5$) epilayers with a rocksalt structure on MgO(001) substrates. These epilayers exhibited cathodoluminescence (CL) near the band edge, particularly in the deep ultraviolet (DUV) region, underscoring the material's potential for advanced optoelectronic applications.

The quest for the most stable and low-enthalpy structures within the MgZnO alloy system has led to the identification of a novel thermodynamically stable compound, Mg_3ZnO_4, crystallizing in a Caswellsilverite-like structure within the rocksalt phase [32]. This discovery was facilitated by an evolutionary algorithm approach, implemented within the Materials Project Database [33]. The Mg_3ZnO_4 compound, characterized by its space group $Pm\bar{3}m$, constitutes a substantial leap forward in the understanding of MgZnO alloys. The identification and characterization of this material were achieved using ab-initio methods, specifically the Quantum ESPRESSO plane-wave computational package [34].

Despite the growing interest in $Mg_xZn_{1-x}O$ alloys and the recent discovery of Mg_3ZnO_4, there remains a notable gap in the literature regarding a comprehensive exploration of the structural, optoelectronic, mechanical, and thermodynamic properties of Mg_3ZnO_4, particularly using advanced ab-initio methods. To our knowledge, no prior studies have utilized the FP-LAPW method combined with the Tran–Blaha modified semi-local Becke–Johnson potential (TB-mBJ) [23] in the WIEN2k computational code to investigate these properties. This study aims to bridge that gap by offering a detailed prediction and analysis of these properties for Mg_3ZnO_4 in its rocksalt configuration, contributing valuable insights to the ongoing development of optoelectronic materials. It is well known that first-principles methods are effective for analyzing the structural and physical properties of solids at the electronic level [35]. The present study aims to address this gap by providing a detailed prediction and analysis of these properties for Mg_3ZnO_4 in its rocksalt configuration, by the first-principles calculations (FP-LAPW) as implemented in WIEN2k code.

This paper is structured as follows: Sect. 2 offers a detailed overview of the computational methods and approaches employed in this research. Section 3 presents the main results, accompanied through a thorough examination of the analyzed ground-state properties, offering insights into their implications for optoelectronic applications. Finally, Sect. 4 presents a summary of the key findings and conclusion drawn from this study, outlining potential directions for future research.

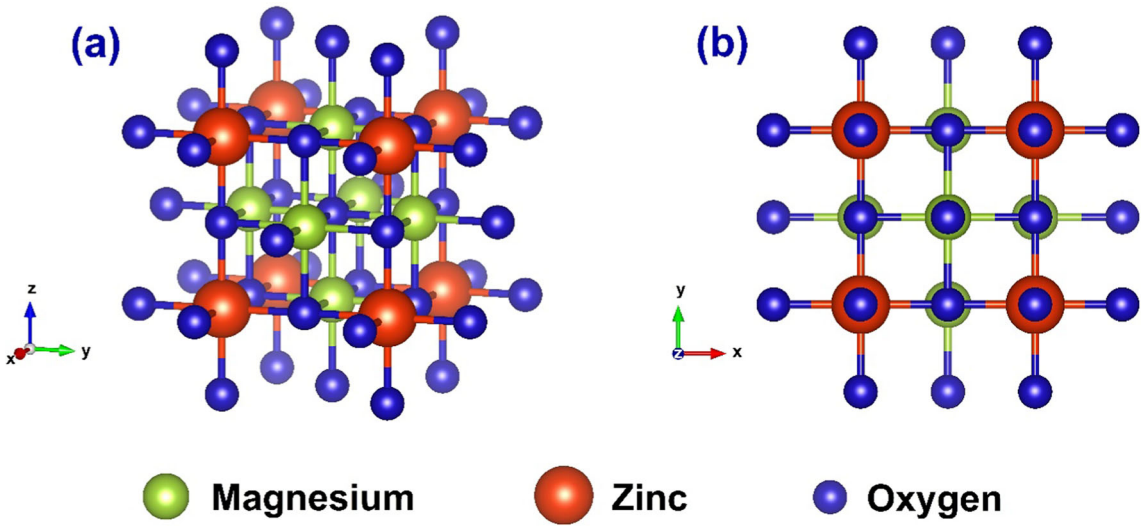

Fig. 1 Crystal structure of Mg_3ZnO_4 in rocksalt structure (cubic, $Pm\bar{3}m$, 221), **a** (111)—plane and **b** (110)—plane

2 Computational details

The calculations for this study were performed using the FP-LAPW method, as implemented in the WIEN2k computational code [36, 37]. This method was employed to conduct total energy calculations and analyze the physical characteristics of the rocksalt phase of Mg_3ZnO_4. In this approach, the unit cell is divided into non-overlapping muffin-tin spheres centered around the atomic sites, with the interstitial regions treated separately. This division allows for the application of different basis sets in each region, providing a flexible and accurate computational framework. The Kohn–Sham equations, derived from (DFT) [38, 39], were solved iteratively to achieve self-consistency in the calculations.

The crystal structure of Mg_3ZnO_4, resembling that of Caswellsilverite, crystallizes in the rocksalt (cubic) phase with the space group $Pm\bar{3}m$ (no. 221). This structure is illustrated in Fig. 1, which presents the (111) plane in panel (a) and the (110) plane in panel (b). Detailed information regarding the geometric arrangements, including atomic positions and lattice parameters, is provided in Tables 1 and 2, along with references [32] and [40] for further context.

For the exchange–correlation potential, various approximations were considered, including the LDA [17], the revised Perdew–Burke–Ernzerhof for solids (PBEsol-GGA) [41], and the GGA of Wu and Cohen (WC-GGA) [22], particularly for calculating the structural properties. To enhance the accuracy of the calculated energy gap values for the rocksalt Mg_3ZnO_4, we utilized LDA, PBEsol-GGA, WC-GGA, the Engel-Vosko GGA approach (EV-GGA) [19], and the semi-local Becke–Johnson potential along with its modified form suggested by Tran and Blaha (TB-mBJ) [23]. It is important to note that the elastic and thermodynamic properties were computed exclusively using the LDA.

Table 1 Atomic positions in the cubic unit cell for Mg_3ZnO_4

Material	Phase	Atom	Atomic positions (x, y, z)
Mg_3ZnO_4	Cubic (rocksalt)	Mg_1	(0, 1/2, 1/2)
		Mg_2	(1/2, 0, 1/2)
		Mg_3	(1/2, 1/2, 0)
		Zn_1	(0, 0, 0)
		O_1	(1/2, 0, 0)
		O_2	(0, 1/2, 0)
		O_3	(0, 0, 1/2)
		O_4	(1/2, 1/2, 1/2)

To enhance the precision of our calculations, the TB-mBJ method was utilized to compute both the imaginary and real components of the dielectric function, as well as other linear optical parameters of the ternary Mg_3ZnO_4 compound in its rocksalt phase. The TB-mBJ potential, introduced by Tran and Blaha [23], provides a more accurate representation of semiconductors and insulators than traditional approximations. This potential offers improved accuracy in modeling the electronic structure, particularly for optical properties. The TB-mBJ potential is expressed as [42]

$$\upsilon_{x,\sigma}^{mBJ}(r) = c\upsilon_{x,\sigma}^{\mathrm{BR}}(r) + (3c-2)\frac{1}{\pi}\sqrt{\frac{5}{12}\sqrt{\frac{2\tau_\sigma(r)}{\rho_\sigma(r)}}}. \quad (1)$$

Table 2 Calculated lattice constant (a), bulk modulus (B), first pressure derivative (B'), equilibrium volume (V_0), minimal energy ($E_{\min}$), and the percent error (Δa) according to LDA, PBEsol-GGA, and WC-GGA for Mg_3ZnO_4 compared with other theoretical works

Mg_3ZnO_4	a [Å]	B [GPa]	B'	V_0 [a.u]^3	$E_{\min}$[Ryd]	Δa [%]
Present results (LDA)	4.1822	182.7762	4.6095	493.6402	− 5383.404052	− 0.423
Present results (PBEsol-GGA)	4.2352	164.2879	4.3821	512.6387	− 5389.811992	+ 0.838
Present results (WC-GGA)	4.2366	164.5422	4.3802	513.1653	− 5394.180532	+ 0.817
Other calculations	4.20 [32] 4.28 [40]	180.4 [32]	–	499.9627 [32]	–	–

In this context, ρ_σ denotes the electron density, τ_σ refers to the kinetic energy, and $\upsilon_{x,\sigma}^{\mathrm{BR}}$ represents the Becke–Roussel potential [43]. Notably, a system-specific parameter, c, embodies the Becke–Johnson potential with its original value set as $c = 1$. Nevertheless, for bulk materials, Tran and Blaha [23] proposed a method to calculate this parameter [21, 42].

In this context, ρ_σ represents the electron density, τ_σ denotes the kinetic energy, and $\upsilon_{x,\sigma}^{\mathrm{BR}}$ signifies the Becke–Roussel potential [43]. A key element of this method is the system-specific parameter c, which is associated with the Becke–Johnson potential and initially set to $c = 1$. However, for bulk materials, Tran and Blaha [23] introduced a procedure to compute this parameter more accurately [21, 42]

$$c = \alpha + \beta\left(\frac{1}{V_{\mathrm{cell}}}\int\frac{|\nabla\rho_\sigma(r')|}{\rho_\sigma(r')}d^3r'\right)^{\frac{1}{2}}. \qquad (2)$$

In this expression, V_{cell} denotes the volume of the unit cell, while the parameters α (− 0.012) and β (1.023) bohr$^{1/2}$ are fitting constants derived from experimental data [23]. The TB-mBJ potential is particularly significant in electronic structure calculations for solids, as it plays a key role in improving band gap accuracy [42, 44]. This raises the question: How does the TB-mBJ potential physically enhance the energy gap by modifying the exchange–correlation potential (V_{xc}), especially in relation to electron behavior and orbital interactions? It is well known that incorporating Hartree–Fock (HF) exchange into the energy functional can meaningfully influence the energy band gap of solids. This effect is evident in the two extremes: pure HF exchange typically overestimates the energy band gap, whereas LDA or GGA functionals within DFT tend to underestimate it. This contrast highlights the importance of hybrid exchange–correlation (XC) functionals, which incorporate a fraction of HF exchange, in providing a more accurate calculation of energy band gaps.

The plane-wave expansion was configured with $R_{\mathrm{MT}} \times K_{\mathrm{MAX}} = 9$, where R_{MT} is the smallest Muffin-Tin radius, and K_{MAX} represents the maximum K-vector within the Brillouin Zone (BZ). For the Mg_3ZnO_4 ternary material under study, the Muffin–Tin radii were set to 1.91, 2.05, and 1.77 atomic units (a.u.) for magnesium (Mg), zinc (Zn), and oxygen (O), respectively. The cut-off for the Fourier-expanded charge density was determined at $G_{\max} = 12$ (a.u.)$^{-1}$. Additionally, the spherical harmonic expansion within the non-overlapping Muffin-Tin spheres was analyzed up to $l_{\max} = 10$. A cut-off energy of − 6 Ryd was established to clearly separate core states from valence states. For the calculations addressing the structural and electronic properties of the Mg_3ZnO_4 compound, a k-point mesh consisting of 56 special k-points (corresponding to a grid of 10 × 10 × 10 meshes, which equates 1000 k-points) was employed to cover the irreducible wedge of the BZ. In contrast, for the linear optical property calculations, a finer k-mesh with 3000 k-points (a grid of 14 × 14 × 14, equivalent to 120 special k-points) was utilized to achieve the necessary precision. This dense mesh of eigenvalues and associated eigenvectors was critical for accurately predicting the linear optical properties. Moreover, the electronic configurations were specifically treated as valence electrons for each element: Mg as $1s^2\ 2s^2\ 2p'\ 3s^2$, Zn as $1s^2\ 2s^2\ 2p'\ 3s^2\ 3p'\ 3d^{10}\ 4s^2$, and O as $1s^2\ 2s^2\ 2p^4$.

3 Results and discussion

This section is dedicated to an in-depth examination of the structural, optoelectronic, mechanical and thermodynamic properties of the ternary compound Mg_3ZnO_4, focusing on its stability and behavior in the rocksalt (cubic) phase. Through this analysis, we intend to elucidate the fundamental characteristics that define the material's potential for various applications, particularly in the realm of optoelectronics. By exploring these properties in detail, we provide critical insights into the compound's suitability for use in advanced technological applications, such as UV photodetectors and thin-film solar cells.

3.1 Geometry and volume optimization

In recent years, high-pressure research has garnered increasing attention, with a particular focus on structural phase transformations and the behavior of materials under compression. This field has garnered significant attention due to its ability to offer deeper

insights into the fundamental theories governing the solid state. Geometry and volume optimization of crystals are fundamental tools for understanding, predicting, and designing materials with desired physical properties, making them indispensable in materials science and engineering research.

To characterize the structural properties of Mg_3ZnO_4, we utilized Murnaghan's equation of state (EOS) [45] to analyze the relationship between total energy (E) and volume (V). This approach enabled us to derive key structural constants, namely the equilibrium lattice parameter (a), the bulk modulus (B), and the first pressure derivative of the bulk modulus (B′).

The EOS fitting was performed using theoretical data obtained from the Materials Project [40], which provided the necessary input parameters for the volume optimization process. We employed various approximations, including the LDA, PBEsol-GGA, and WC-GGA, to compute these structural constants.

In Murnaghan's equation (Eq. 3), E_0 represents the equilibrium total energy of the material, B_0 is the bulk modulus indicating the material's resistance to compression, and $B_0{}'$ denotes the first derivative of the bulk modulus with respect to pressure. By fitting the EOS to the total energy versus volume data, we obtained accurate estimates of these parameters, providing valuable insights into the mechanical and structural stability of the Mg_3ZnO_4 compound

$$E(V) = E_0 + \frac{B_0 V}{B_0'}\left(\frac{(V_0/V)^{B_0'}}{B_0' - 1} + 1\right) - \frac{B_0 V_0}{B_0' - 1}. \tag{3}$$

To determine the structural parameters of Mg_3ZnO_4, we analyzed the total energy versus volume curves using various approximations: LDA, PBEsol-GGA, and WC-GGA. These calculations allowed us to derive key structural parameters—namely the equilibrium lattice parameter a, B, and B'. Figure 2 illustrates the total energy–volume curves and the corresponding fitted parameters obtained from these approximations.

The minimized values for a, B, and B' computed from LDA, PBEsol-GGA, and WC-GGA approximations are presented in Table 2, alongside comparisons with previous theoretical data [32, 40]. Our results indicate that the lattice parameter a calculated using the LDA approach is slightly underestimated by approximately 0.423% compared to prior theoretical values [32]. Conversely, the PBEsol-GGA and WC-GGA methods result in overestimations of a by approximately 0.838% and 0.817%, respectively. These discrepancies highlight the sensitivity of lattice parameter predictions to the choice of approximation and underline the need for careful consideration of functional selection in theoretical studies.

In terms of the B and its pressure derivative B', our results align well with previously reported theoretical works. The agreement suggests that the LDA, PBEsol-GGA, and WC-GGA approximations provide a reliable depiction of the material's compressibility and its response to pressure changes. Despite the absence of experimental data for these structural constants of Mg_3ZnO_4, our theoretical findings offer a valuable reference point for future experimental investigations. The consistency with the existing theoretical results enhances the credibility of our predictions and provides a solid foundation for further experimental and theoretical research.

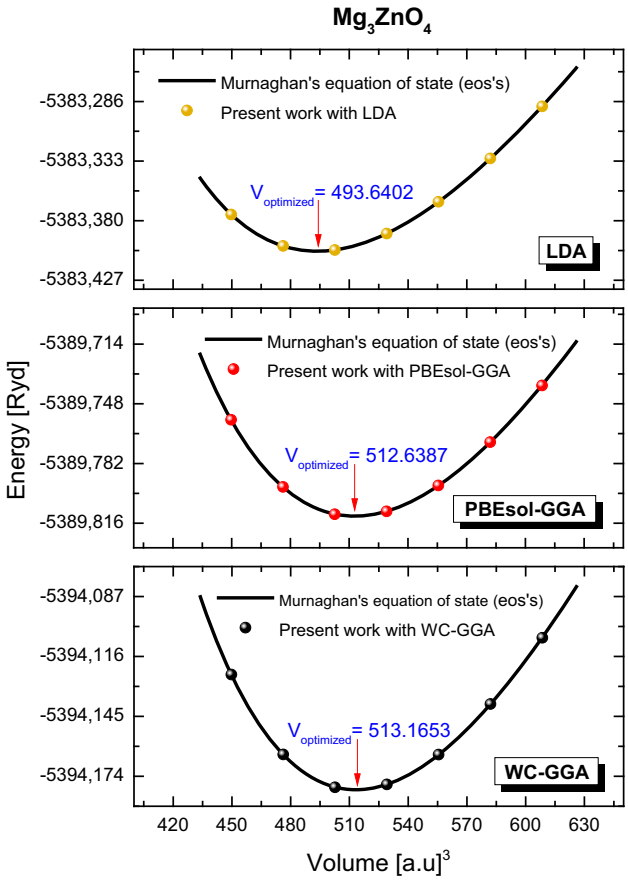

Fig. 2 Calculated total energy as a function of unit cell volume for Mg_3ZnO_4 within LDA, PBEsol-GGA, and WC-GGA approximations

3.2 Electronic properties

Understanding electronic properties, such as band structure and density of states (DOS), is crucial for optimizing materials in various electronic applications. The electronic band structure provides insights into the energy levels available to electrons, while the density of states reveals how these levels are occupied. The semiconductor band gap, which is a key factor in determining a material's suitability for electronic devices, is influenced by the material's atomic arrangement and symmetry. These factors dictate how the band energy levels are populated around the E_F [42].

In this study, we computed the energy band-gap values for Mg_3ZnO_4 in its rocksalt cubic phase using

Table 3 Calculated band gap (Eg) within LDA, WC-GGA, EV-GGA, and TB-mBJ approximations for Mg_3ZnO_4 compared with other theoretical works

Mg_3ZnO_4	E_g [eV]					
Approximations	LDA	WC-GGA	PBEsol-GGA	EV-GGA	TB-mBJ using LDA	TB-mBJ using GGA
Present works	2.456	2.217	2.217	3.033	4.668	4.476
Other works	5.95 [32], 2.83 [40]					

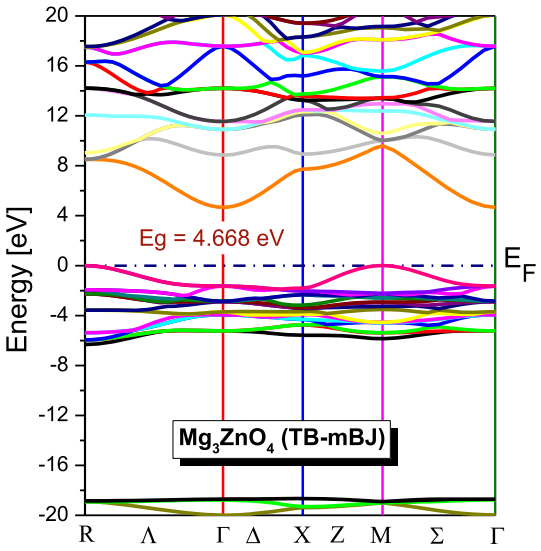

Fig. 3 Band structure of Mg_3ZnO_4 within TB-mBJ approximation

several computational approaches: LDA, PBEsol-GGA, WC-GGA, EV-GGA, and the Tran–Blaha modified Becke–Johnson potential (TB-mBJ). The results from these methods are summarized in Table 3. Although all approaches provided valuable insights, we focus here on the results obtained using the TB-mBJ method. This is because the TB-mBJ approach offers a more accurate representation of the energy band gap, capturing subtle electronic characteristics that are critical for understanding the material's performance in electronic devices. The patterns observed across different methods are consistent, reinforcing the reliability of the TB-mBJ results in characterizing the electronic properties of Mg_3ZnO_4.

Figure 3 presents the band structure of Mg_3ZnO_4, as calculated using the TB-mBJ approximation, spanning an energy range from − 20 to 20 eV along the high-symmetry directions $R \rightarrow \Gamma \rightarrow X \rightarrow M \rightarrow \Gamma$ in the Brillouin Zone (BZ). This band structure analysis reveals that the minima of the conduction band and the maxima of the valence band occur at different k-points, which is characteristic of an indirect band gap. When the E_F is positioned at 0 eV, this indirect band gap is evident, meaning that electronic transitions between the valence and conduction bands involve a change in momentum. Such a band structure has implications for the material's optical properties and its effectiveness in various electronic and optoelectronic applications.

Table 3 summarizes the band-gap values (E_g) for Mg_3ZnO_4 obtained using several computational approaches, including LDA, WC-GGA, EV-GGA, and TB-mBJ. These values are compared with those from prior theoretical studies. The TB-mBJ approach, in particular, predicts a higher band gap compared to the other methods. This enhancement can be attributed to TB-mBJ's refined treatment of the exchange–correlation potential (V_{xc}). The TB-mBJ method incorporates a portion of Hartree–Fock (HF) exchange, which corrects the underestimation of the band gap that occurs with pure HF exchange and the typical underestimation of LDA or GGA functionals. By blending HF exchange with local or gradient-corrected exchange–correlation terms, TB-mBJ provides a more accurate band gap, underscoring its importance in the precise calculation of electronic properties.

In our study, we calculated the band gap for Mg_3ZnO_4 using the modified Becke–Johnson (mBJ) potential, yielding a value of 4.668 eV. This value is lower than the 5.95 eV reported in reference [32] and higher than the 2.83 eV in reference [40]. These differences arise from the methodologies used in the respective studies. Reference [32] employed the Local Density Approximation (LDA), which often underestimates band gaps, while reference [40] used the Generalized Gradient Approximation (GGA), which also yields lower values. The mBJ method, which incorporates a portion of Hartree–Fock exchange, provides a more accurate representation of electronic properties. Furthermore, our calculations indicate that the cubic structure is the most stable form of Mg_3ZnO_4. The calculated band gap of 4.668 eV emphasizes Mg_3ZnO_4's potential for optoelectronic applications, particularly in the ultraviolet region.

Figure 4 illustrates the band gap of Mg_3ZnO_4 as determined by the TB-mBJ method in relation to the solar spectrum, including AM0 and AM1.5 irradiance conditions. As definition, the AM0 provides a baseline for maximum solar energy in space, while AM1.5 simulates real-world conditions for solar panels on Earth, ensuring standardized testing for comparing solar cell efficiency and performance. The solar spectrum is divided into visible (380–750 nm), infrared (IR), and ultraviolet (UV) regions. The computed band

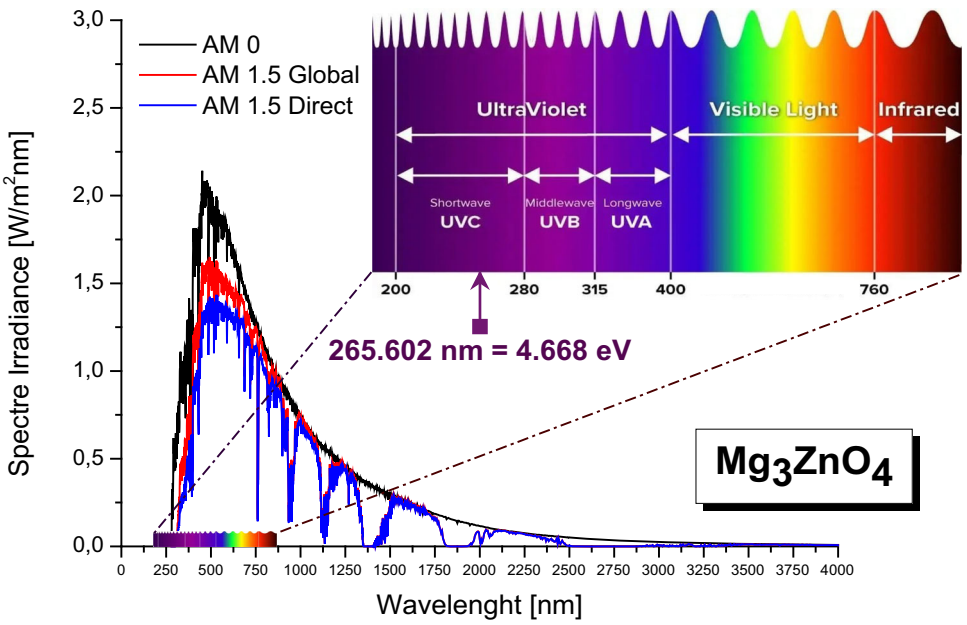

Fig. 4 The spectrum of sun's solar radiation versus photon energy values of Mg_3ZnO_4 with the positioning of the *Eg* within TB-mBJ approximation

gap of 4.668 eV indicates that Mg_3ZnO_4 has substantial absorption in the UV region, specifically at a wavelength of 265.602 nm (shortwave UVC). This characteristic suggests that Mg_3ZnO_4 could be effectively used in UV optoelectronic applications, where materials with high-energy band gaps are desirable for absorbing high-energy photons.

To elucidate the interplay between atomic orbitals and electronic band structures in Mg_3ZnO_4, we examine the projected total density of states (TDOS) and partial density of states (PDOS) calculated using the TB-mBJ method. Figure 5 presents the PDOS for each type of atom in Mg_3ZnO_4, with the E_F set at 0 eV in all plots. The band gap is identified as the energy range immediately above E_F where no electronic states are present.

In Fig. 5, the DOS is organized into three distinct regions: the low-energy valence band (VB_{low}), the higher energy valence band (VB_{higher}), and the conduction band (C_B). The VB_{low}, which is primarily influenced by oxygen s-orbitals (O_s), spans from − 20.07 to − 18.49 eV. This region reflects the lower energy states predominantly occupied by electrons in the valence band. The VB_{higher}, which is shaped by zinc d-orbitals (Zn_d) and oxygen *p*-orbitals (O_p), extends from − 6.36 to 0 eV. This higher energy valence band features states that contribute to the band's width and electronic properties near the Fermi level. The conduction band (C_B), ranging from 4.67 to 23 eV, is largely characterized by magnesium *s*- and *p*-orbitals (Mg_s and Mg_p). This band's width and position relative to the valence bands are crucial for determining the material's electronic and optical behavior.

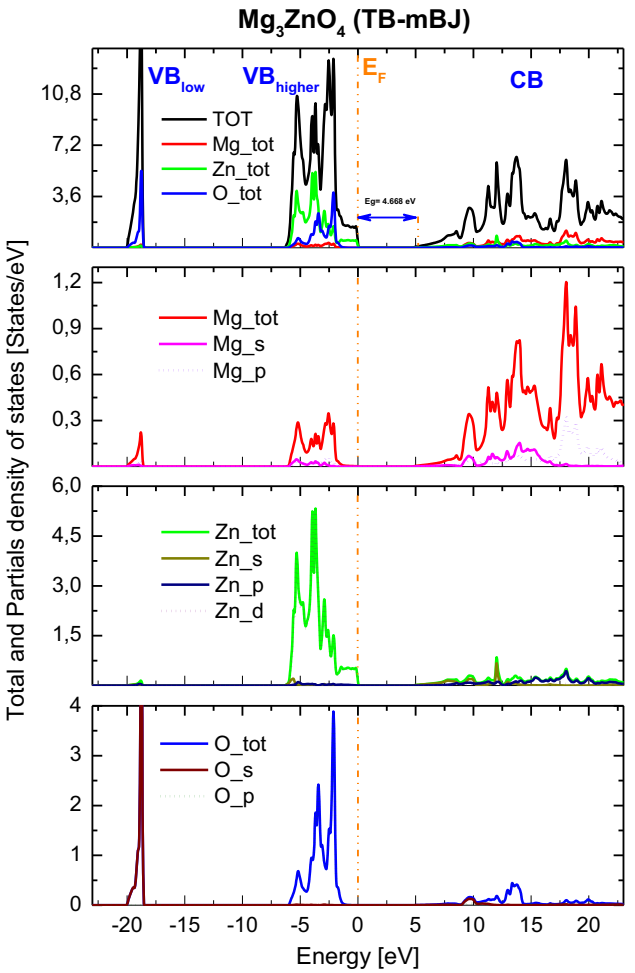

Fig. 5 Partial and total density of states (PDOS and TDOS) of Mg_3ZnO_4 within TB-mBJ approximation

The TDOS reveals that the overall density of states in Mg_3ZnO_4 is predominantly derived from the contributions of magnesium atoms. This distribution of electronic states is instrumental in understanding the material's electronic structure and its potential applications in various optoelectronic devices [46].

3.3 Optical properties

The study of optical properties is crucial for driving technological innovations in fields, such as optoelectronics, medical diagnostics, and environmental sensing. Understanding these properties not only facilitates the development of cutting-edge materials for energy applications but also enhances our capabilities in nanotechnology and device fabrication. In this research, we meticulously calculated the linear optical properties of the Mg_3ZnO_4 compound, focusing on key parameters such as the dielectric function, absorption coefficient, reflectivity, refractive index, optical conductivity, and electron energy-loss spectrum. These calculations were performed using the Tran–Blaha modified Becke–Johnson (TB-mBJ) potential, chosen for its effectiveness in accurately optimizing the band gap of the material. The band gap plays a critical role in determining the optical behavior of materials, making the TB-mBJ approximation particularly suitable for this study. A finely tuned k-point mesh was employed, consisting of 3000 k-points, corresponding to a grid of 14 × 14 × 14, which is equivalent to 120 special k-points, to ensure high precision in the results. Additionally, a broadening parameter of 0.1 eV was applied in the calculations to account for potential smearing effects and to achieve more accurate representations of the material's optical spectra [47].

The dielectric function, $\varepsilon\ (\omega)$ describes the response of a material to an external electric field at a given frequency ω. It is generally a complex function, expressed as: $\varepsilon(\omega) = \varepsilon_{\text{real}}(\omega) + i\ \varepsilon_{\text{imaginary}}(\omega)$ [44, 48–57]. The real part of the dielectric function aids in determining other linear optical parameters, such as the absorption coefficient $a(\omega)$, reflectivity $R(\omega)$, refractive index $n(\omega)$, optical conductivity $\kappa(\omega)$, and energy-loss function $L(\omega)$. The joint density of states and momentum matrix elements facilitate understanding interband transitions between the valence band (VB) and conduction band (CB), which are crucial for calculating $\varepsilon_{\text{imaginary}}(\omega)$ [57]. The $\varepsilon_{\text{imaginary}}(\omega)$ is defined by the following relation [44]:

$$\varepsilon_{\text{imaginary}}(\omega) = \frac{e^{2\hbar}}{\pi m^2 \omega^2} \sum \int \left[|M_{c,v}(k)|^2 \delta\left[\omega_{c,v}(k) - \omega\right]\right] d^3k. \tag{4}$$

The integral is evaluated across the entire Brillouin zone (BZ), where $M_{c,v}(k)$ symbolizes the dipole moment associated with direct electronic transitions between the valence band (VB) and the conduction band (CB). The transition energy, denoted as $\omega_{c,v}(k) = E_{ck} - E_{vk}$, represents the energy difference between the conduction band and valence band at a given wave vector k. To calculate the real part of the dielectric function, $\varepsilon_{\text{real}}(\omega)$, the Kramers–Kronig relations are employed, which allow for the determination of the dielectric response from the material's complex optical properties. This integral approach is crucial for accurately capturing the optical behavior of materials, particularly in the context of direct inter-band transitions, which play a significant role in determining the optical spectra. The Kramers–Kronig relations provide a robust framework for connecting the real and imaginary parts of the dielectric function, ensuring that the results adhere to the principles of causality and are physically meaningful [44, 53]

$$\varepsilon_{\text{real}}(\omega) = 1 + \frac{2}{\pi} p \int_0^{\infty} \frac{\varepsilon_{\text{imaginary}}(\omega')}{\omega'^2 - \omega^2} \mathrm{d}\omega'. \tag{5}$$

The optical properties, such as the absorption coefficient $\alpha(\omega)$, reflectivity $R(\omega)$, refractive index $n(\omega)$, extinction coefficient $\kappa(\omega)$, and electron energy-loss function $L(\omega)$, can be systematically derived from the real and imaginary components of the dielectric function. These properties are interconnected through specific mathematical relations, allowing for a comprehensive understanding of the material's optical response across different frequencies. By applying these established formulas, we can accurately calculate and analyze each optical property, providing insight into how the material interacts with electromagnetic radiation. This approach is critical for evaluating the material's potential applications in various optoelectronic and photonic devices, where precise control over optical behavior is essential [44, 53, 55, 57–59]

$$\alpha(\omega) = \sqrt{2}\omega\left[\sqrt{\varepsilon_{\text{real}}^2(\omega) + \varepsilon_{\text{imaginary}}^2(\omega)} - \varepsilon_{\text{real}}(\omega)\right] \tag{6}$$

$$R(\omega) = \left[\sqrt{[\varepsilon_{\text{real}}^2(\omega) + i\varepsilon_{\text{imaginary}}(\omega) - 1]} / \sqrt{[\varepsilon_{\text{real}}^2(\omega) + j\varepsilon_{\text{imaginary}}(\omega) + 1]}\right]^2 \tag{7}$$

$$n(\omega) = \frac{1}{\sqrt{2}} \sqrt{\left[\left[\varepsilon_{\text{real}}^2(\omega) + \varepsilon_{\text{imaginary}}^2(\omega)\right]^{\frac{1}{2}} + \varepsilon_{\text{real}}(\omega)\right]} \tag{8}$$

$$\kappa(\omega) = (-i\omega/4\pi)\varepsilon(\omega) \tag{9}$$

$$L(\omega) = \mathrm{Im}\left(-\frac{1}{\varepsilon(\omega)}\right) = \frac{\varepsilon_{\text{imaginary}}(\omega)}{\varepsilon_{\text{real}}^2(\omega) + \varepsilon_{\text{imaginary}}^2(\omega)}. \tag{10}$$

3.3.1 Dielectric function

Figures 6 and 7 illustrate the variation of the real and imaginary components of the dielectric function for

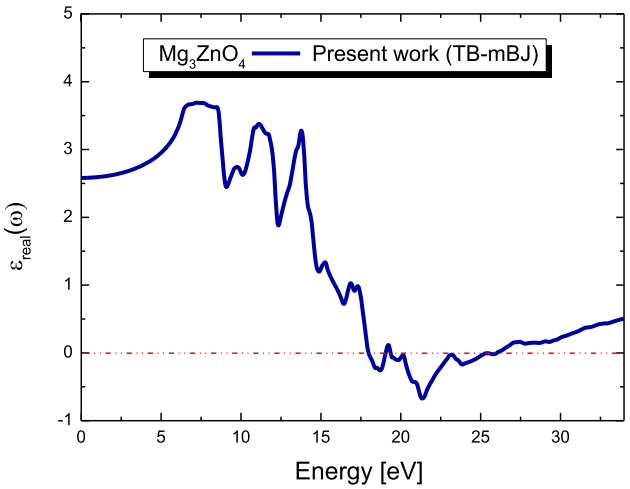

Fig. 6 Computed real part of the dielectric function for Mg_3ZnO_4 using the TB-mBJ approximation

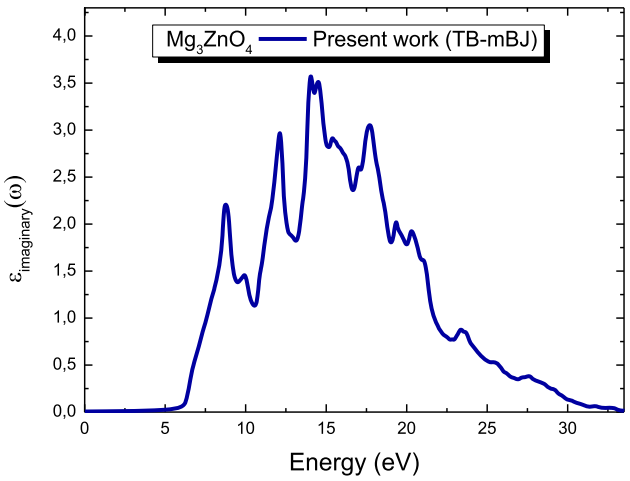

Fig. 7 Computed imaginary part of the dielectric function for Mg_3ZnO_4 using the TB-mBJ approximation

Mg_3ZnO_4 as a function of photon energy, ranging from 0 to 35 eV. The zero-frequency limit, $\varepsilon_{\text{real}}(0)$, is a crucial parameter that is intrinsically linked to the material's energy band gap, as highlighted in the previous studies [53]. The static dielectric constant $\varepsilon_{\text{real}}(0)$, calculated using the Tran–Blaha modified Becke–Johnson (TB-mBJ) approximation, is presented in Table 4. Notably, $\varepsilon_{\text{real}}(\omega)$ remains positive up to a photon energy of 17.99 eV under polarization conditions, beyond which it becomes negative, indicating a change in the material's optical behavior. Prominent peaks in the real part of the dielectric function are observed at photon energies of 7.224, 7.605, 11.115, and 13.782 eV, corresponding to electronic transitions from the valence band to the conduction band.

The imaginary part of the dielectric function, $\varepsilon_{\text{imaginary}}(\omega)$, calculated using the TB-mBJ approximation, reveals various inter-band transitions between occupied and unoccupied electronic states within the material. As depicted in Fig. 7, the imaginary component exhibits several peaks in response to incident photon energy up to 35 eV. For Mg_3ZnO_4, four major peaks are identified: the first occurs at 8.748 eV, followed by subsequent peaks at 12.122, 14.054, and 17.701 eV. These peaks are primarily attributed to the hybridization between the bonding and anti-bonding states involving O_s/p and Mg_s/p orbitals, reflecting the complex electronic interactions within the material.

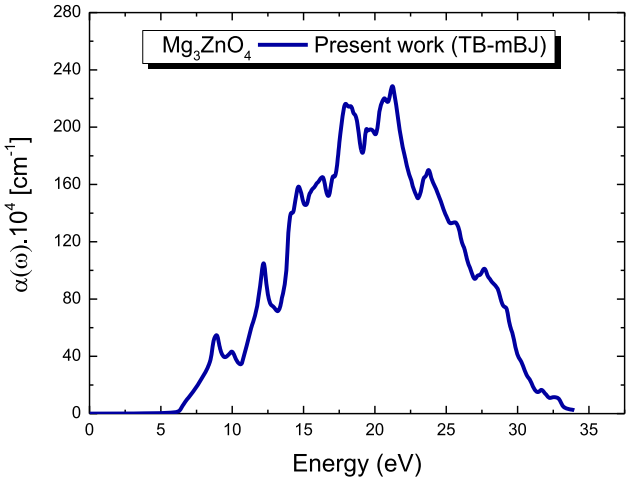

Fig. 8 Computed absorption coefficient for Mg_3ZnO_4 using the TB-mBJ approximation

3.3.2 Absorption coefficient

The absorption coefficient $\alpha(\omega)$ is a fundamental linear optical parameter that indicates the fraction of light absorbed as it passes through a material. The calculated absorption coefficients for the longitudinal and parallel components of light for Mg_3ZnO_4, determined using the TB-mBJ approximation, are shown in Fig. 8. This figure covers the energy range of incident photons from 0 to 35 eV. It is evident that the compound exhibits excellent optical absorption ($\alpha(\omega)_{\max} = 2.286 \times 10^6$ cm^{-1}) over a wide energy range of 4.672–21.238 eV, corresponding to wavelengths between 58.378 and 265.49 nm, which falls within the

Table 4 Calculated optical dielectric constant, static reflectivity, and static refractive index for Mg_3ZnO_4 within TB-mBJ approximation

Mg_3ZnO_4	Static parameters			
Present work (TB-mBJ)	$\varepsilon_{\text{imaginary}}(0)$	$R(0)$	$n(0)$	$\kappa(\omega)$ peak's
	2.58	16.06	1.606	17.728

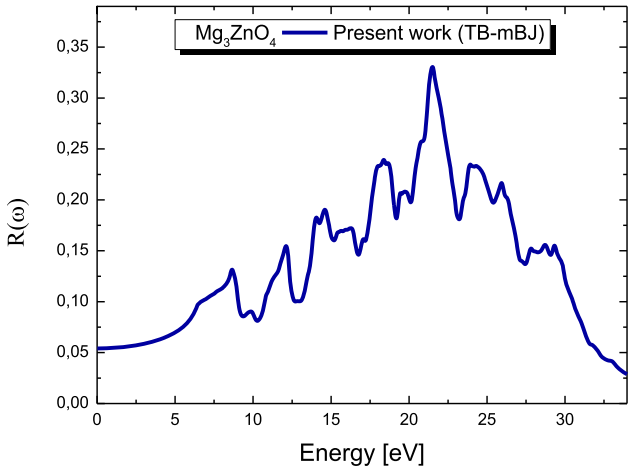

Fig. 9 Computed reflectivity for Mg_3ZnO_4 using the TB-mBJ approximation

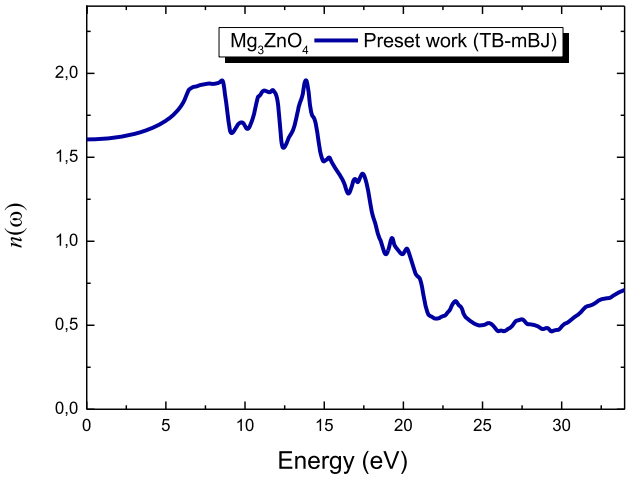

Fig. 10 Computed refractive index for Mg_3ZnO_4 using the TB-mBJ approximation

Ultra–Violet (UV) region. Here, the isotropic behavior in the context of polarization type refers to the uniform response of a material to light, regardless of the direction of the light's electric field. In isotropic materials, the optical properties, such as absorption and refractive index, are the same in all directions. This uniformity leads to a consistent interaction with light, independent of its polarization. For the compound Mg_3ZnO_4, the isotropic behavior means that the material absorbs light equally well across different polarization states. This results in a harmonious trend in the optical absorption characteristics, as the material's response does not vary with the polarization of the incident light. Therefore, the calculated absorption coefficients for both longitudinal and parallel components of light show similar patterns, indicating the material's isotropic nature. Observations indicate that Mg_3ZnO_4 is well suited for applications requiring absorption of light in the UV region of the solar spectrum. Therefore, Mg_3ZnO_4 can be used in optoelectronic devices (UV photodetectors, LEDs, laser diodes), photovoltaic cells for enhanced solar efficiency, UV-sensitive sensors, UV-driven catalytic processes, and protective coatings to shield materials from UV radiation.

3.3.3 Reflectivity

Reflectivity $R(\omega)$ is a crucial parameter in the analysis of linear optical properties, as it quantifies the ratio of the intensity of reflected light to that of incident light as a function of angular frequency ω. This optical property provides critical insight into how much light is reflected from the surface of a material at various frequencies or photon energies. $R(\omega)$ is particularly significant, because it is highly sensitive to the intricate interactions between the real and imaginary components of the dielectric function, making it an essential indicator of how a material interacts with electromagnetic radiation, especially at semiconductor surfaces.

Figure 9 presents the reflectivity spectra of Mg_3ZnO_4 over a range of photon energies, calculated using the TB-mBJ functional. This analysis reveals how the reflectivity varies with photon energy, offering valuable information about the material's optical response. Additionally, the zero-frequency reflectivity $R(0)$, which represents the reflectivity at the limit of low frequencies, is provided in Table 4, derived from the TB-mBJ calculations. The maximum reflectivity for Mg_3ZnO_4, as shown in Fig. 9, occurs at a photon energy of 21.51 eV, corresponding to a wavelength of approximately 0.0576 μm (57.638 nm). This peak reflectivity indicates the energy at which the material most effectively reflects incident light, which is important for applications requiring specific reflective properties.

3.3.4 Refractive index

The refractive index $n(\omega)$ is a fundamental parameter for understanding atomic-level interactions in semiconducting materials. It serves as an indicator of the material's transparency across different wavelengths of spectral radiation and is critical for predicting its performance in optoelectronic applications. Generally, materials with higher refractive indices tend to exhibit reduced transparency due to increased absorption and scattering of light, whereas those with lower refractive indices allow for greater light transmission, thereby enhancing transparency.

Figure 10 illustrates the calculated refractive index $n(\omega)$ for Mg_3ZnO_4 across photon energies up to 35 eV, revealing three significant peaks at 8.53, 11.741, and 13.837 eV, all of which fall within the ultraviolet (UV) region. These peaks indicate specific energy levels where the material exhibits notable refractive behavior. The static refractive index n(0), which represents the refractive index at zero frequency, is given by $n(0) = \sqrt{\varepsilon_{\text{imaginary}}(0)} = 1.606$ and has been derived using the TB-mBJ approximation. This value is listed in Table 4, providing a reference for the material's refractive properties at low frequencies.

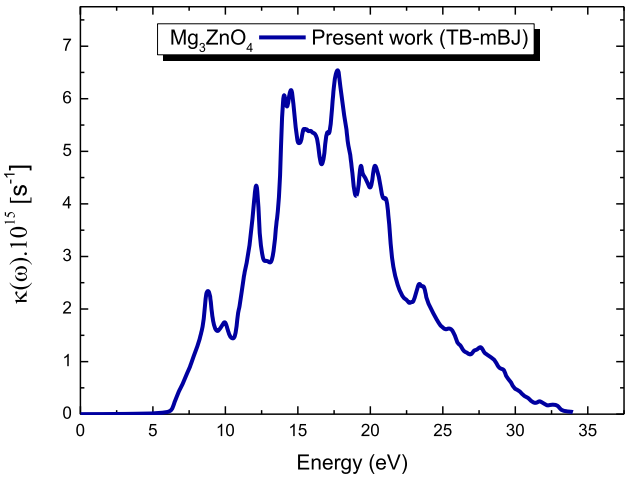

Fig. 11 Computed conductivity for Mg_3ZnO_4 using the TB-mBJ approximation

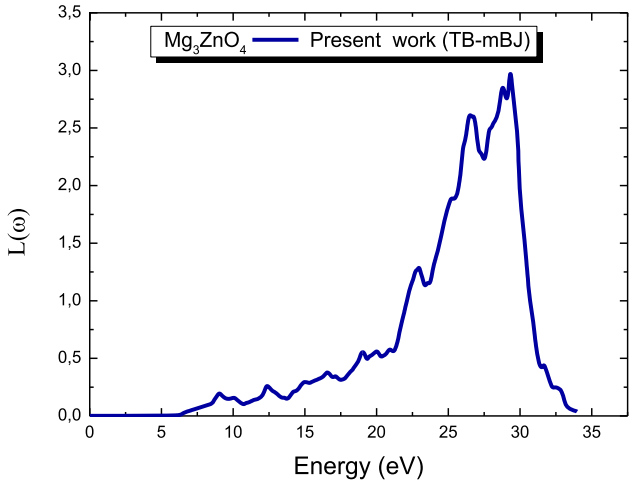

Fig. 12 Computed energy-loss function for Mg_3ZnO_4 using the TB-mBJ approximation

3.3.5 Optical conductivity

Optical conductivity $\kappa(\omega)$ is a key parameter that indicates how effectively a material conducts electricity when exposed to light of varying frequencies or energies. It reveals the material's electronic response to incident photons across the electromagnetic spectrum, which is crucial for understanding and optimizing its optoelectronic properties. This parameter is directly derived from the dielectric function, as outlined in Eq. 9.

Figure 11 presents the optical conductivity $\kappa(\omega)$ for Mg_3ZnO_4, calculated up to a photon energy of 35 eV using the TB-mBJ approximation. The graph highlights several significant peaks in the optical conductivity, which correspond to critical interactions within the material. These peaks are indicative of bulk plasmon excitations, representing the collective oscillations of electrons between the valence band (VB) and the conduction band (CB). The specific locations of the highest optical conductivity peaks are detailed in Table 4, with the most prominent peak corresponding to a value of 6.54×10^{15} s^{-1}. This information is essential for applications, such as photodetectors, solar cells, and optoelectronic devices.

3.3.6 Electron energy-loss function

The electron energy-loss function $L(\omega)$ represents the energy dissipated by a fast-moving electron as it interacts with a material, providing essential insights into the electronic structure of the material. This spectrum is particularly valuable for analyzing the material's optical and electronic properties, as it encompasses interactions across the entire energy spectrum, including those involving both elastically scattered and non-scattered electrons. The energy-loss function is sensitive to interactions that lead to the excitation of electrons, whether through inter-band transitions within the valence band or from the outer atomic shells [21].

Figure 12 presents the calculated energy-loss function $L(\omega)$ for Mg_3ZnO_4, obtained using the TB-mBJ approach. The spectrum highlights a critical point at 29.32 eV, which corresponds to the region where the material experiences minimal energy loss, often referred to as a lossless region. This region is of particular interest in the study of material properties, as it indicates energy ranges where the material can sustain electronic excitations with minimal resistance.

3.4 Mechanical properties

Understanding the elastic properties of a solid is fundamental for analyzing its mechanical and dynamic responses under various conditions. These properties—such as Young's modulus, shear modulus, and Poisson's ratio—quantify how a material deforms under applied stresses and are crucial for predicting its behavior in real-world applications. Elasticity reflects how a material returns to its original shape after deformation, which is vital for determining its structural integrity and load-bearing capacity.

Elastic properties are not only important for assessing the mechanical strength of materials but also play a significant role in understanding their thermal and dynamic behaviors. For instance, the interplay between elastic constants and thermal expansion coefficients can influence the material's performance in high-temperature environments, where thermal stresses might lead to significant deformations or failure. Additionally, the ability of a material to absorb and dissipate energy, which is governed by its elastic moduli, affects its vibrational characteristics and stability under dynamic loading conditions.

By examining these properties, one gains insights into the internal forces and stress distributions within the material. This information is essential for evaluating the material's capacity to withstand mechanical forces, vibrations, and thermal stresses without undergoing permanent deformation or failure. Consequently, a thorough understanding of elastic properties is crucial

for designing and optimizing materials for structural applications, where mechanical stability and durability are paramount [60].

3.4.1 Elastic constants

Elastic constants are crucial in correlating the macroscopic mechanical properties of materials with their microscopic behavior, offering profound insights into the material's stiffness and crystal stability. These constants act as fundamental parameters that describe how a material deforms under applied forces, and they play a significant role in characterizing the material's mechanical response at different scales. Hooke's law provides a fundamental framework for understanding this relationship between strain and stress. Mathematically, Hooke's law is expressed as $\sigma_{ij} = \epsilon_{kl}\ C_{ijkl}$, where σ_{ij} represents the stress components, ϵ_{kl} denotes the strain components, and C_{ijkl} is the fourth-rank elastic stiffness tensor. The tensor C_{ijkl} encapsulates the material's elastic constants and defines how stress is related to strain within the material. In the realm of lattice dynamics, Hooke's law can be adapted to incorporate lattice symmetry, which is particularly relevant for single crystals such as Mg_3ZnO_4. When applied to these materials, the elastic constants help describe how the crystal lattice responds to mechanical perturbations. Specifically, they characterize the stress–strain relationship within the crystal structure, capturing how the lattice deforms in response to external forces and how these deformations affect the material's stability.

By analyzing the elastic constants in the context of lattice dynamics, we can gain a deeper understanding of the material's mechanical properties, such as its rigidity, stability, and resistance to deformation. This understanding is essential for predicting the material's performance under various conditions and for designing materials with tailored mechanical properties. Thus, the study of elastic constants provides critical insights into the fundamental mechanical behavior of materials and their suitability for diverse applications [61, 62]. When Hooke's law is applied to lattice dynamics with lattice symmetry, the stress–strain relationship for Mg_3ZnO_4 single crystals can be illustrated in the following form:

$$\begin{pmatrix} \sigma_1 \\ \sigma_2 \\ \sigma_3 \\ \tau_1 \\ \tau_2 \\ \tau_3 \end{pmatrix} = \begin{pmatrix} C_{11} & C_{12} & C_{13} & 0 & 0 & 0 \\ C_{21} & C_{22} & C_{23} & 0 & 0 & 0 \\ C_{31} & C_{32} & C_{33} & 0 & 0 & 0 \\ 0 & 0 & 0 & C_{44} & 0 & 0 \\ 0 & 0 & 0 & 0 & C_{55} & 0 \\ 0 & 0 & 0 & 0 & 0 & C_{66} \end{pmatrix} \begin{pmatrix} \epsilon_1 \\ \epsilon_2 \\ \epsilon_3 \\ \gamma_1 \\ \gamma_2 \\ \gamma_3 \end{pmatrix}. \tag{11}$$

Here, γ_i, ϵ_i, τ_i, and σ_i show the shearing strain, normal strain, corresponding shearing stress, and the normal stress, respectively. The elastic flexibility matrix S_{ij} can be illustrated as the inverse of the elastic stiffness matrix C_{ij}, i.e., $[S_{ij}] = [C_{ij}]^{-1}$. For a cubic crystal, due to lattice symmetry, there are three independent variables in S_{ij}: S_{11}, S_{12}, S_{44} and C_{ij}: C_{11}, C_{12}, C_{44}. In this study, the elastic constant calculated for the cubic Mg_3ZnO_4 crystal structure is summarized in Table 5, with the calculated values of S_{11}, S_{12}, and S_{44} being 0.0034, − 0.00085, and 0.0075, respectively.

For cubic structures (rocksalt phase), three independent second-order elastic constants are observed. Particularly, the C_{11}, C_{12}, and C_{44} elastic constants of

Table 5 The elastic constants (C_{11}, C_{12}, C_{44}), the bulk modulus (B), the shear modulus (G_V, G_R, G_H), the anisotropy factor (A), the melting temperature (T_{melt}), Young's modulus (E_V, E_R, E_H), Poisson's ratios (σ_V, σ_R, σ_H), the B_H/G_H ratio, the percent shear factor A_G, and the universal elastic anisotropy index A^U for Mg_3ZnO_4 within LDA approximation

(Mg_3ZnO_4)	Present results (LDA)		Other results [32]
Elastic constants	C_{11} (GPa)	346.4276	316.9
	C_{12} (GPa)	113.4690	112.1
	C_{44} (GPa)	131.6540	132.1
	S_{11} (GPa)	0.0034	–
	S_{12} (GPa)	− 0.00085	–
	S_{44} (GPa)	0.0075	–
Bulk modulus	B (GPa)	191.1218	180.4
Shear modulus	G_V (GPa)	125.5841	–
	G_R (GPa)	125.133	–
	G_H (GPa)	125.3586	–
Poisson's ratios	σ_V	0.230	–
	σ_R	0.231	–
	σ_H	0.230	–
Young's modulus	E_V (GPa)	309.056	–
	E_R (GPa)	308.147	–
	E_H (GPa)	308.602	–
Ratio	B_H/G_H	1.5246	–
Anisotropy factor	A	1.1302	–
Melting temperature	T_{melt} (K)	2600.3871 ± 300	–
Percent shear factor	A_G %	0.1798	–
Universal elastic anisotropy index	A^U %	0.0179	–
Bulk modulus anisotropy index	$A_{Bc} = A_{Ba}$	1	–

Mg_3ZnO_4 with a $Pm\bar{3}m$ crystal symmetry are listed in Table 5. These elastic constants can be calculated using LDA approximation. To evaluate the elastic stability of cubic structures, the "Born stability criteria" [63, 64] is necessary and can be determined using the following equations [65]:

$$C_{11} > 0; C_{11} - C_{12} > 0; C_{11} + 2C_{12} > 0; \\ C_{44} > 0 \text{ and } C_{12} < B < C_{11}. \quad (12)$$

Considering these elastic constants, the determined values represented in Table 5 meet all the aforementioned restrictions. Moreover, Mg_3ZnO_4 compound has been considered mechanically stable at room temperature and pressure, which was confirmed in Ref. [32]. From our calculations, it has been observed that C_{11} is greater than all other constants, showing that our material has further resistance to change in length than in volume and shape. Additionally, the $< 100 >$ directions are the densest and stiffest in terms of structure.

The bulk modulus (B) is a compound's resistance to volumetric compression under applied pressure. Essentially, B is eligible to quantify the necessary energy to generate deformation [60]. To calculate B, Pugh's (B_V) and Reuss's bulk modulus (B_R) equations can be employed [66]

$$B_V = \frac{(C_{11} + 2C_{12})}{3} \quad (13)$$

$$B_R = \frac{1}{3S_{11} + 6S_{12}}. \quad (14)$$

Here, with both temperature and pressure at zero, the obtained value of B for the considered Mg_3ZnO_4 compound is 191.1218 GPa. This result is fairly reliable with the value of 182.7762 GPa calculated using Murnaghan's equation of state (EOS) with the LDA approximation. The Voigt [67] and Reuss [68] methods are used to calculate the shear modulus (G) from the elastic constants. These include calculating the Voigt shear modulus (G_V) and the Reuss shear modulus (G_R)

$$G_V = \frac{C_{11} - C_{12} + 3C_{44}}{5} \quad (14)$$

$$G_R = \frac{15}{4S_{11} - 4S_{12} + 3S_{44}}. \quad (15)$$

Hill [69] represented that G_V is the Voigt shear modulus and G_R is the Reuss shear modulus, showing the upper and lower restrictions of G, respectively. He also indicated that the Navier [70] equation could be used to calculate the G_H-average

$$G_H = G = \frac{G_V + G_R}{2}. \quad (16)$$

Moreover, Young's modulus (E) and Poisson's ratio (σ) are calculated using the calculated values of compressibility modulus and shear modulus, which are replaced into the following formulas [71–74]:

$$E = \frac{9BG}{3B + G} \quad (17)$$

$$\sigma = \frac{3B - 2G}{2(3B + G)}. \quad (18)$$

Pugh [66] proposed a simple equation, known as Pugh's ratio (B/G) [66], to estimate the brittleness and ductility of compounds. A B/G ratio less than 1.75 shows brittleness (fragility), while a B/G ratio greater than 1.75 shows ductility [75, 76]. According to Table 5, the estimated value of the B/G ratio determined using the LDA estimation gives a B/G ratio of 1.5246, representing that Mg_3ZnO_4 is a fragile compound.

Moreover, Frantsevich et al. [77] suggested using Poisson's ratio (σ) to distinguish between ductile and brittle behavior in materials. σ assists not only as a sign of a compound's compressibility but also as a sign of bonding forces characteristics. The Poisson's ratio can effectively differentiate between brittle and ductile compounds: a higher Poisson's ratio ($\sigma > 0.26$) shows ductility, while a lower value ($\sigma < 0.26$) represents brittleness [78].

As represented in Table 5, the σ_H value for our structure is 0.23 as determined using LDA approximation, verifying its fragility. The Poisson's ratio also allows us to calculate the type of bond in the crystal structure. According to Haines et al. [79], σ is 0.1 for covalent materials, 0.25 for ionic materials, and 0.33 for metallic materials. The Poisson's ratio determined for Mg_3ZnO_4 is close to 0.25, representing an ionic bond material. An ionic bond material involves the presence of chemical bonds generated between atoms when one atom gives one or more electrons to another atom, resulting in the formation of cations and anions.

Young's modulus (E) is the essential characteristic of solids, representing the relationship between stress–strain and determining the stiffness of the materials. As described in Table 5, the ternary compound (Mg_3ZnO_4) is classified as fragile, as evidenced by its determined value of 308.602 GPa Young's modulus using the LDA function.

The hardness can be calculated according to Vickers using the below equation [80]

$$H_v = 0.92\left(\frac{G}{B}\right)^{1.3137} \times G^{0.708}. \quad (19)$$

According to [81], it has been reported that materials with a Vickers hardness value larger than 40 GPa are considered super hard materials. Given that the calculated H_v for Mg_3ZnO_4 is 16.17 GPa, it is expected that Mg_3ZnO_4 exhibits exceptional resistance to denting and scratching.

3.4.2 Elastic anisotropy

The universal anisotropic index A^U [82] and the percent anisotropy indexes of shear and compression (A_G and A_B) [83] explain the elastic anisotropy indexes. The calculation equations are depicted below

$$A^U = 5\frac{G_V}{G_R} + \frac{B_V}{B_R} - 6 \tag{20}$$

$$A_B = \frac{B_V - B_R}{B_V + B_R} \tag{21}$$

$$A_G = \frac{G_V - G_R}{G_V + G_R}. \tag{22}$$

Elastic anisotropy plays an essential role in understanding the mechanical behavior of materials under stress, particularly when subjected to different crystallographic directions. The degree of anisotropy influences various properties, such as fracture toughness, thermal conductivity, and mechanical durability, which are essential for potential applications, especially in optoelectronics and thin-film technologies.

Upon calculations, the universal anisotropy index (A^U) for Mg_3ZnO_4 was found to be 0.018, indicating that Mg_3ZnO_4 exhibits nearly isotropic behavior. In isotropic materials, the mechanical properties are identical in all directions, while deviations from isotropy can lead to differences in material performance depending on the direction of applied stress. The low AU value suggests that Mg_3ZnO_4 maintains mechanical uniformity, which is advantageous for applications requiring consistent mechanical responses across different orientations.

In terms of compression, the bulk modulus anisotropy (A_B) was calculated to be 0, demonstrating that Mg_3ZnO_4 experiences isotropic compression. This means that when pressure is applied uniformly, the material compresses equally in all directions, indicating that the bonding strength between atoms is homogeneous. Such behavior is critical in high-pressure environments where uniform compression is desired, as it reduces the risk of mechanical failure or distortion.

The shear anisotropy (A_G) value of 0.0017 further reinforces that Mg_3ZnO_4 has almost isotropic shear behavior. This suggests that the shear response is nearly the same along different planes, which is crucial for materials that undergo shear stresses during deformation. The calculated shear anisotropy values provide insights into the directional bonding strength, particularly how atomic bonds behave under non-uniform forces across different crystallographic planes. In materials with higher shear anisotropy, these bonds could exhibit different strengths in various directions, potentially leading to uneven deformation or cracking under stress.

The shear anisotropy factor of A_1, A_2, and A_3 in the [100], [010], and [001] planes, respectively are expressed as follows [83]:

$$A_1 = \frac{4C_{44}}{C_{22} + C_{33} - 2C_{13}} \tag{23}$$

$$A_2 = \frac{4C_{55}}{C_{33} + C_{11} - 2C_{23}} \tag{24}$$

$$A_3 = \frac{4C_{66}}{C_{11} + C_{22} - 2C_{12}}. \tag{25}$$

To determine the elastic anisotropy of cubic single crystals, one method is to calculate the Zener constant (A), which is appropriate and expressed by the following equation [67, 68]:

$$A = \frac{2C_{44}}{C_{11} - C_{12}}. \tag{26}$$

For isotropic crystals, the shear anisotropy factor is conventionally 1, with deviations from this value indicating varying degrees of shear anisotropy [84]. The specific shear anisotropy factor of 1.13 for Mg_3ZnO_4 in the [100], [010], and [001] planes highlights a moderate level of anisotropy in these directions. While this value is not significantly higher than 1, it indicates that Mg_3ZnO_4 has slightly stronger shear resistance in these directions, suggesting that the material might behave more rigidly under shear stress along certain planes. This is particularly relevant for applications that involve mechanical processing or deformation, as it provides clues about how the material will behave under operational conditions.

Furthermore, the anisotropic indices of the bulk modulus along the c- and a-axes can be expressed using Eqs. (27) and (28), respectively [83]. These equations quantify the directional dependence of the bulk modulus, providing insights into how the material's resistance to volume changes varies with orientation

$$A_{Bc} = \frac{(C_{11} - C_{12})(C_{33} - C_{13}) - (C_{23} - C_{13})(C_{11} - C_{13})}{(C_{33} - C_{13})(C_{22} - C_{12}) - (C_{13} - C_{23})(C_{12} - C_{23})} \tag{27}$$

$$A_{Ba} = \frac{(C_{22} - C_{12})(C_{11} - C_{13}) - (C_{11} - C_{12})(C_{23} - C_{12})}{(C_{22} - C_{12})(C_{33} - C_{13}) - (C_{12} - C_{23})(C_{13} - C_{23})}. \tag{28}$$

In the realm of elastic properties, the anisotropy index serves as a pivotal parameter for characterizing the degree of elastic isotropy within crystalline materials. A unit value of this index signifies complete isotropy, wherein the elastic response remains uniform across all crystallographic directions. Deviations from this unit value indicate varying levels of anisotropic behavior, where directional dependence arises in the material's mechanical response. For the Mg_3ZnO_4 crystal, the calculated anisotropy indices for the bulk modulus, A_{Bc} and A_{Ba}, are both found to equal 1. This outcome confirms that the bulk modulus of Mg_3ZnO_4 is isotropic, suggesting that the material exhibits equivalent resistance to volumetric changes irrespective of the direction of applied pressure.

The isotropy of the bulk modulus is significant for theoretical modeling and practical applications, as it implies a consistent mechanical behavior under hydrostatic stress conditions, thus facilitating predictable performance in a variety of operational environments. Moreover, this uniformity enhances the reliability of Mg_3ZnO_4 in structural applications, particularly in optoelectronic devices where uniform mechanical integrity is critical. The absence of directional dependence in the bulk modulus also simplifies the analysis of stress distributions and failure mechanisms, enabling more accurate assessments of material performance in engineering applications. Thus, the isotropic nature of Mg_3ZnO_4's bulk modulus positions it as a favorable candidate for applications demanding high mechanical reliability and consistent elastic behavior.

To further investigate the isotropic characteristics of the Mg_3ZnO_4 crystal, a 3D surface representation of elastic anisotropy was performed. The directional dependencies of both Young's modulus and the bulk modulus within the cubic crystal system are detailed in Eqs. (29) and (30), respectively [85]. These equations provide insights into how the material's elastic properties vary with direction and confirm the observed isotropy in the bulk modulus, while also exploring any potential anisotropy in Young's modulus

$$\frac{1}{E} = S_{11} - 2\left(S_{11} - S_{12} - \frac{S_{44}}{2}\right)\left(l_1^2 l_2^2 + l_2^2 l_3^2 + l_1^2 l_3^2\right) \tag{29}$$

$$\frac{1}{B} = (S_{11} + 2S_{12})\left(l_1^2 + l_2^2 + l_3^2\right). \tag{30}$$

For the Mg_3ZnO_4 crystal, the bulk modulus B exhibits isotropy across the lattice directions (x, y, and z), as illustrated in Fig. 13. The three-dimensional (3D) surface representation of Young's modulus also confirms this isotropy, with the surface appearing spherical. In materials science, isotropy implies that the material's properties are uniform in all directions, which is visually represented by a spherical shape of the 3D surface plot.

In the case of Mg_3ZnO_4, Young's modulus exhibits a low degree of anisotropy, as illustrated in Fig. 13. The minimum value of Young's modulus, measured at 290.436 GPa, is observed along the $< 111 >$ crystal direction, while the maximum value of 321.204 GPa is found along the $< 100 >$ direction. These values, along with their corresponding anisotropy ratio (E_{max}/E_{min}), which quantifies the degree of directional dependence, are summarized in Table 6. The calculated anisotropy ratio of 1.1 indicates that the material possesses relatively low anisotropy in Young's modulus [86]. Furthermore, the three-dimensional (3D) representation of Young's modulus, shown in Fig. 13, confirms a near-spherical shape, characteristic of materials exhibiting low anisotropy. This slight variation in stiffness suggests that Mg_3ZnO_4 will maintain relatively uniform mechanical properties across different crystallographic directions.

A more detailed examination of Young's modulus, which reflects the material's resistance to deformation, reaffirms the minimal anisotropy indicated by the anisotropy ratio of 1.1. The minimum value of 290.436 GPa along the $< 111 >$ direction and the maximum value of 321.204 GPa along the $< 100 >$ direction indicate some degree of directional dependence, although this is relatively minor. The near-spherical 3D surface of Young's modulus, as confirmed in Fig. 13, further supports the concept of uniform stiffness. Such a low degree of anisotropy implies that Mg_3ZnO_4 is well suited for applications requiring consistent mechanical performance, such as thin-film optoelectronic devices or flexible electronics, where uniform stiffness across various orientations is crucial for optimal functionality.

The 3D surface representation of the shear modulus for Mg_3ZnO_4 can be expressed using Eq. (30) [87], further detailing the material's directional dependency in shear response

$$\frac{1}{G} = (S_{44} + 4SJ) \tag{30}$$

$$S = S_{11} - S_{22} - \frac{S_{44}}{2}, \tag{31}$$

where

$$J = \sin^2\theta.\cos^2\theta + 0.125.\sin^4\theta(1 - \cos 4\varphi). \tag{32}$$

The analysis of the shear moduli of the Mg_3ZnO_4 crystal along various orientations reveals a notable degree of anisotropy, as illustrated in Fig. 13. The minimum shear modulus, measured at 121.134 GPa, is consistently observed along the $< 100 >$, $< 010 >$, and $< 001 >$ directions. In contrast, the maximum value reaches 131.654 GPa along the $< 111 >$ direction, highlighting the crystal's directional dependence. This variation suggests that the material exhibits higher rigidity and resistance to shear deformation along the $< 111 >$ direction compared to the $< 100 >$, $< 010 >$, and $< 001 >$ directions. Such behavior implies that the atomic bonding characteristics in Mg_3ZnO_4 differ depending on the crystallographic orientation, which may arise from the underlying crystal structure and the arrangement of atoms within the lattice.

To quantify this anisotropy in shear modulus, we can use the ratio of the maximum to minimum shear modulus values, denoted as G_{max}/G_{min}, which is listed in Table 6. For Mg_3ZnO_4, this ratio is calculated to be 1.086, indicating a slight but significant variation in shear rigidity across different orientations. Generally, the directional dependence of the shear modulus tends to be inversely related to that of Young's modulus, suggesting that the material exhibits distinct mechanical behaviors in different crystallographic directions (Fig. 14).

This anisotropic behavior of the shear modulus has important implications for the material's mechanical performance, particularly in applications subjected to torsional or shear forces. The higher shear modulus

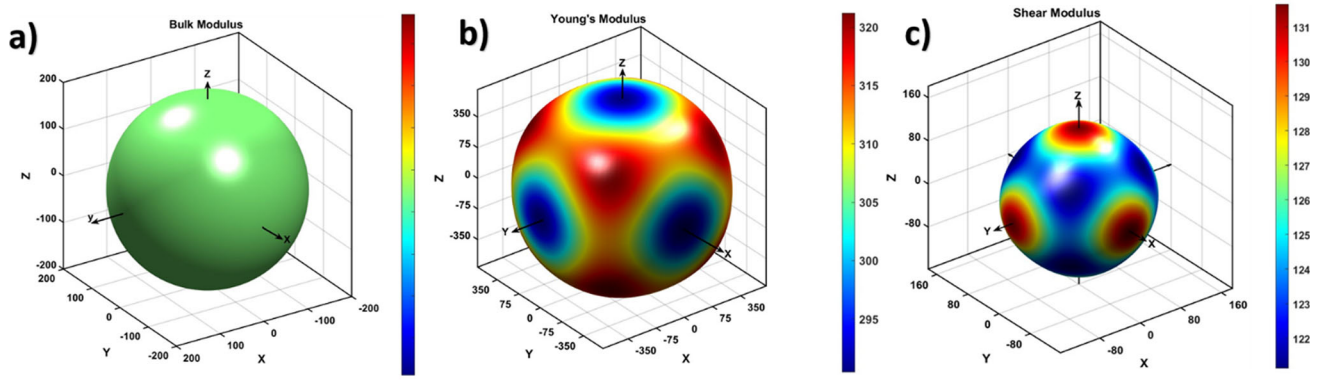

Fig. 13 Directional dependence of **a** bulk modulus, **b** shear modulus, and **c** Young's modulus of Mg3ZnO4 crystal

Table 6 Maximum and minimum and anisotropy ratios of Young's modulus E and shear modulus G in *xy*, *xz*, and *yz* perspective planes of Mg_3ZnO_4 crystal

		xy	*xz*	*yz*
Young's modulus	E_{max} (GPa)	321.204	321.204	321.204
	E_{min} (GPa)	290.436	290.436	290.436
	Anisotropic ratio *A*	1.1	1.1	1.1
Shear modulus	G_{max} (GPa)	131.654	131.654	131.654
	G_{min} (GPa)	121.134	121.134	121.134
	Anisotropic ratio *A*	1.09	1.09	1.09

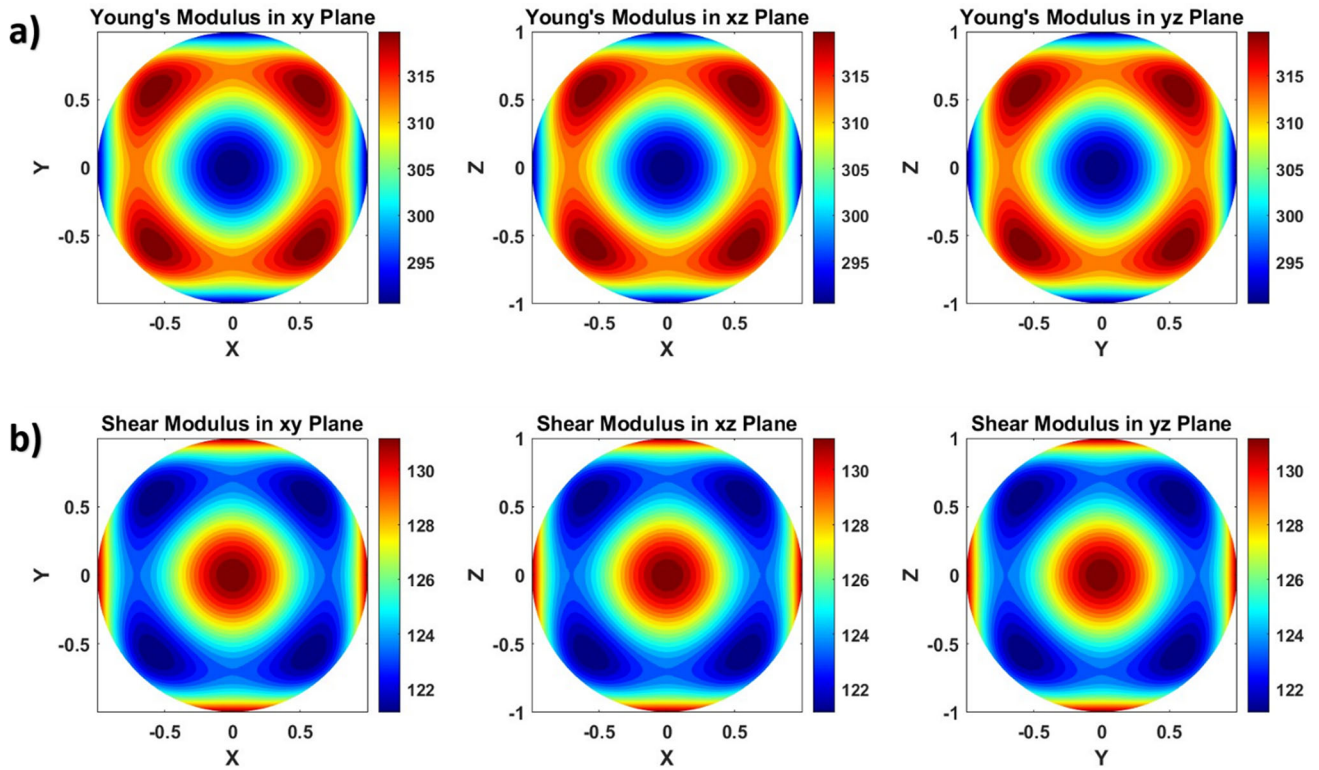

Fig. 14 The counterplot of the plane perspective of **a** Young's modulus E and **b** shear modulus G in *xy*, *xz*, and *yz* planes of Mg_3ZnO_4 crystal

along the < 111 > direction indicates that Mg_3ZnO_4 is relatively more resistant to shear deformation in that orientation. Such characteristics could influence how the material behaves under stress, potentially leading to different failure modes depending on the orientation of applied forces. Understanding these anisotropic properties is crucial for optimizing the material's use in applications, such as thin-film optoelectronic devices or flexible electronics, where mechanical reliability and performance under varying loading conditions are paramount.

Additionally, the anisotropy of Poisson's ratios was examined by calculating values along three low-index planes. For a cubic crystal, the Poisson's ratio ν along arbitrary directions in the (hkl) planes can be depicted as described by Zhang [88]

$$\nu(hkl,\,\theta) = \left\{ S_{12} + \frac{S}{(h^2+k^2+l^2)} \left[\left(\frac{h^2 l}{\sqrt{h^2+k^2}.\sqrt{h^2+k^2+l^2}} \cos\theta - \frac{hk}{\sqrt{h^2+k^2}} \sin\theta \right)^2 \right. \right. \\ \left. \left. + \left(\frac{k^2 l}{\sqrt{h^2+k^2}.\sqrt{h^2+k^2+l^2}} \cos\theta + \frac{hk}{\sqrt{h^2+k^2}} \sin\theta \right)^2 + \left(\frac{l\sqrt{h^2+k^2}}{\sqrt{h^2+k^2+l^2}} \cos\theta \right)^2 \right] \right\} / \\ \left[-S_{11} + 2S \frac{(hk)^2 + (hl)^2 + (lk)^2}{(h^2+k^2+l^2)^2} \right]. \tag{33}$$

The variations in Poisson's ratios across different crystallographic planes of Mg_3ZnO_4 reveal significant insights into its mechanical anisotropy. As depicted in Fig. 15, the Poisson's ratios for the low-index planes (100) and (111) are calculated to be 0.247 and 0.1934, respectively. These values indicate minimal directional dependence in these planes, suggesting that the material exhibits relatively uniform behavior when subjected to tensile or compressive stresses in these orientations. In practical terms, this implies that when the material is stretched or compressed, its lateral expansion or contraction will be nearly the same across the (100) and (111) planes, which is beneficial for applications requiring consistent mechanical performance.

In contrast, the (110) plane exhibits more pronounced anisotropy, with Poisson's ratios ranging from 0.1884 to 0.2658. Specifically, the minimum Poisson's ratio of 0.1884 is observed along the $[\bar{1}10]$ direction, while the maximum value of 0.2658 is found along the $[00\bar{1}]$ direction. This notable variation highlights the directional dependence of the material's mechanical responses within the (110) plane, indicating that its properties are more sensitive to the orientation of applied stresses compared to the (100) and (111) planes. Such sensitivity suggests that the material may experience different degrees of lateral deformation under identical loading conditions, potentially affecting its mechanical reliability and performance in real-world applications.

A summary of the Poisson's ratios for the three low-index planes of the Mg_3ZnO_4 crystal is presented in Table 7, providing a comprehensive overview of the material's mechanical anisotropy. This information aids in understanding the structural behavior of Mg_3ZnO_4 under various stress conditions. The values indicate that while the low-index planes (100) and (111) exhibit stable and predictable mechanical responses, the (110) plane's variability necessitates careful consideration in design applications, particularly where directional loading may be encountered.

In summary, Poisson's ratio serves as a crucial parameter in assessing the elastic anisotropy of Mg_3ZnO_4. The relatively low and consistent Poisson's ratio values for the (100) and (111) planes reflect a robust and uniform elastic behavior, advantageous for applications that demand reliability across multiple orientations. Conversely, the pronounced anisotropy in the (110) plane underscores the importance of considering directional effects in engineering applications, particularly in contexts where the material is subjected to varying mechanical loads. Mg_3ZnO_4 demonstrates near-isotropic behavior in several of its elastic properties, particularly in terms of its bulk modulus and overall stiffness. However, it also exhibits slight anisotropy in specific shear moduli and Poisson's ratios across certain crystallographic planes. This nuanced mechanical behavior is crucial for applications where directional performance is critical, such as in structural components of optoelectronic devices or in other scenarios requiring high mechanical reliability. Understanding these characteristics allows for optimized design and selection of materials tailored to specific mechanical requirements.

3.4.3 Calculation of Debye temperature

The Debye temperature (θ_D) is essentially correlated with many physical properties of solids, such as elastic constants and melting temperature, and specific heat [83]. One standard approaches to calculate the Debye temperature is using the average sound velocity (v_m) by Eq. (34) [89]

$$\theta_D = \frac{\hbar}{k_B} \left(\frac{3nN_A\rho}{4\pi M} \right)^{\frac{1}{3}} v_m \tag{34}$$

where k_B is Boltzmann's constant, $\hbar$ Planck's constant, ρ is the density, N_A is Avogadro's number, n is the

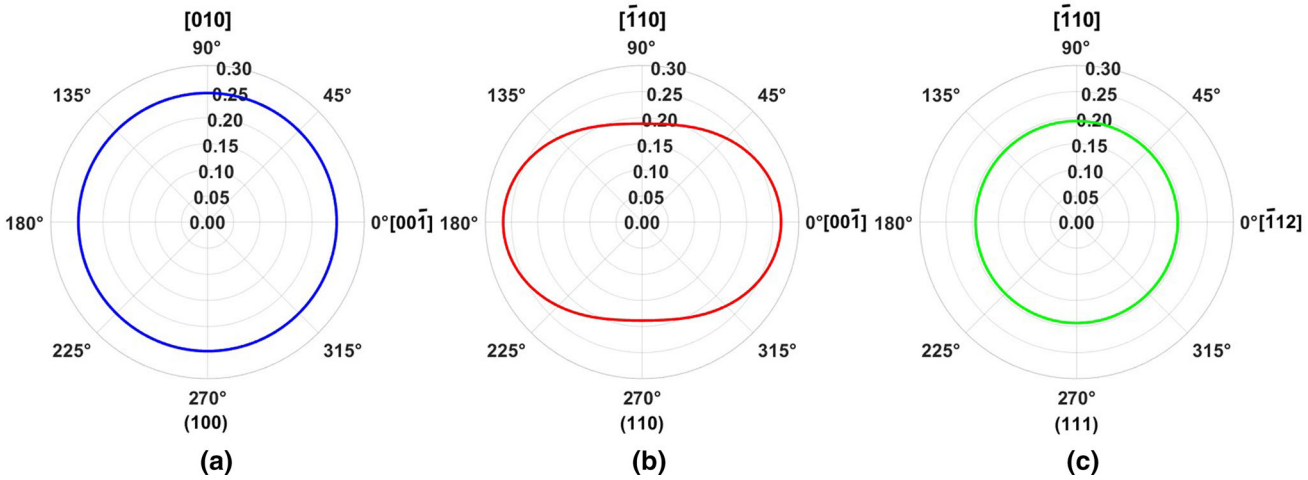

Fig. 15 Direction dependence of Poisson's ratio on low-index planes of Mg_3ZnO_4 crystal: **a** (100), **b** (110), and **c** (111)

Table 7 Poisson's ratios along two orthogonal symmetric directions in three low-index planes of Mg_3ZnO_4 crystal

Planes	(100)		(110)		(111)	
directions	[010]	[00$\bar{1}$]	[$\bar{1}$10]	[001]	[$\bar{1}$10]	[11$\bar{2}$]
Poisson's ratios	0.2470	0.2470	0.2658	0.1884	0.1934	0.1934

number of atoms in a molecule, and M is the molecular weight. The average wave velocity v_m is approximately expressed by the below formulas [89, 90]

$$v_m = \left[\frac{1}{3}\left(\frac{1}{v_l^3} + \frac{2}{v_t^3}\right)\right]^{-\frac{1}{3}} \tag{35}$$

$$v_l = \left(\frac{3B + 4G}{3\rho}\right)^{\frac{1}{2}} \tag{36}$$

$$v_t = \left(\frac{G}{\rho}\right)^{\frac{1}{2}}. \tag{37}$$

Among these parameters, v_t and v_l show the transverse and longitudinal elastic wave velocity of the polycrystalline compound, respectively, determined using shear modulus (G) and bulk modulus (B). The calculated elastic properties are listed in Table 8.

The Debye temperature (θ_D) of 176.42 K offers valuable insights into the thermal and mechanical behavior of the material. A relatively low θ_D indicates substantial atomic vibrations at room temperature, which can significantly influence the material's elastic properties and overall stability. The vibrational modes associated with this Debye temperature suggest that the material may experience notable phonon contributions to its mechanical response, particularly under varying thermal conditions. Increased atomic vibrations can lead to enhanced thermal expansion and reduced stiffness, affecting the material's capacity to withstand mechanical stress. Understanding the implications of θ_D is especially crucial for applications in thermoelectrics and other devices subject to thermal fluctuations, where maintaining the material's mechanical integrity is paramount. Thus, the calculated Debye temperature is not merely a numerical value; it serves as a critical parameter for assessing the material's thermal dynamics and potential performance in practical mechanical applications.

3.5 Thermodynamic properties

Determining thermodynamic properties is crucial for a comprehensive understanding and accurate prediction of a material's behavior under various conditions. These properties encompass aspects such as chemical and thermal stability, mechanical strength, and the evolution of different phases and microstructures. Analyzing thermodynamic data not only aids in optimizing material development processes but also helps in assessing how materials will perform and behave in real-world environments.

In this study, we employed Density Functional Theory (DFT) to calculate the thermodynamic properties of Mg_3ZnO_4. This approach allows us to explore the material's behavior under idealized conditions, with temperature and pressure set to zero, effectively characterizing its ground-state properties. Using this method, we gain insights into the intrinsic characteristics and stability of the material, providing a foundational understanding of its fundamental behavior.

The DFT-based calculations offer a detailed view of how Mg_3ZnO_4 would perform in ideal conditions, contributing valuable information for both theoretical analysis and practical applications. This methodology is instrumental in predicting the material's performance, optimizing its properties for specific uses, and guiding future research and development efforts.

Table 8 The corresponding thermodynamic properties of Mg_3ZnO_4 crystal

Mg_3ZnO_4	ρ[g/cm^3]	v_t[m/s]	v_l[m/s]	v_m[m/s]	θ_D[K]
Present results (LDA)	4.5	166.79	282.24	187.42	176.42

The starting point for explicitly including the effect of temperature and pressure in the calculation is the Gibbs free energy given by the following equation:

$$G = U + \mathrm{PV} + \mathrm{TS}. \tag{38}$$

This equation is the thermodynamic identity that describes the Gibbs free energy (G) of a system. Here is a breakdown of each term in the equation:

G Gibbs free energy, which quantifies the maximum reversible work that a thermodynamic system can perform at constant temperature and pressure. U Internal energy, which is the total energy contained within the system. PV Pressure–volume work, where P is the pressure and V is the volume of the system. T Temperature of the system. S Entropy, which quantifies the disorder or randomness in the system.

Entropy controls the change in Gibbs free energy as temperature varies at constant pressure through

$$\left(\frac{\partial G}{\partial T}\right) = -S. \tag{39}$$

From a microscopic and statistical point of view, entropy quantifies the number of configurations accessible to a system. A phase that offers a greater number of configurations in phase space has a higher probability of being explored, which translates into greater stability. In the context of vibrations, at a temperature of 0 K, the atoms are immobile, which represents a particular configuration. The system gains energy at a rate regulated by the heat capacity at constant volume

$$\left(\frac{\partial G}{\partial T}\right)_V = C_V. \tag{40}$$

The available energy can be used to increase the kinetic energy of the ions, which start to vibrate around their equilibrium position, or to excite the electrons beyond the Fermi level in a metallic material. At low temperature, we observe that the heat capacity is the sum of a linear term in T, attributable to the electrons, and a term in 3 T, attributable to the vibrations of the lattice [91].

3.5.1 Formalism of Debye quasi-harmonic model

To investigate the thermodynamic properties of Mg_3ZnO_4, we employed the Debye quasi-harmonic model, which provides a framework for analyzing the material's behavior under varying temperature and pressure conditions. Using the Gibbs2 program [92], we can determine the Debye temperature (θ_D) and generate the non-equilibrium Gibbs function $G^*(V, P, T)$ from the energy of the solid E as a function of molecular volume V. The minimization of G leads to the thermal equation of state (EOS); $V(P,T)$ and the chemical potential $G(P,T)G(P,\ T)G(P,T)$ of the corresponding phase

$$G^*(V; P, T) = E(V) + PV + A_{vib}[\theta_D; T], \tag{41}$$

where $E(V)$ represents the total energy per unit cell, PV indicates the constant hydrostatic pressure, and $A_{\mathrm{vib}}[\theta_D; T]$ is the vibrational term given by [93, 94]

$$A_{vib}[\theta_D; T] = nkT\left[\frac{9}{8}\frac{\theta_D}{T} + 3ln\left(1 - e^{-\theta_D/T}\right) - D(\theta_D/T)\right]. \tag{42}$$

Here, n denotes the number of atoms per formula unit, $D(\theta_\mathrm{D}/T)$ represents the Debye integral, and for an anisotropic solid [93, 95].

By finding the solution to the Eq. (43)

$$\left(\frac{\partial G^*(V; P, T)}{\partial V}\right)_{P,T} = 0. \tag{43}$$

The isothermal bulk modulus B_T can be obtained as follows [96]:

$$B_T(P, T) = -V\left(\frac{\partial P}{\partial V}\right) = V\left(\frac{\partial^2 G^*(V; P, T)}{\partial V^2}\right)_{P,T}. \tag{44}$$

Based on the quasi-harmonic Debye model, the heat capacity C_v, entropy S, and thermal expansion coefficient α can be derived as follows [96]:

$$C_v = 3nk\left[4D(\theta_D/T) - \frac{3\theta_D/T}{e^{\theta_D/T} - 1}\right] \tag{45}$$

$$S = nk\left[4D(\theta_D/T) - 3ln\left(1 - e^{-\theta_D/T}\right)\right] \tag{46}$$

$$\alpha = \frac{\gamma C_v}{B_T V}, \tag{47}$$

where γ is the Grüneisen parameter.

This approach allowed us to effectively compute the key thermodynamic characteristics of Mg_3ZnO_4 across a broad range of temperatures (0–700 K) and pressures (0–20 GPa). The results will provide insights into the material's stability, heat capacity, and other critical properties as they evolve with changes in temperature and pressure, which is essential for applications where Mg_3ZnO_4 is subjected to diverse environmental conditions. In the following section, we will present these results in detail and discuss their implications.

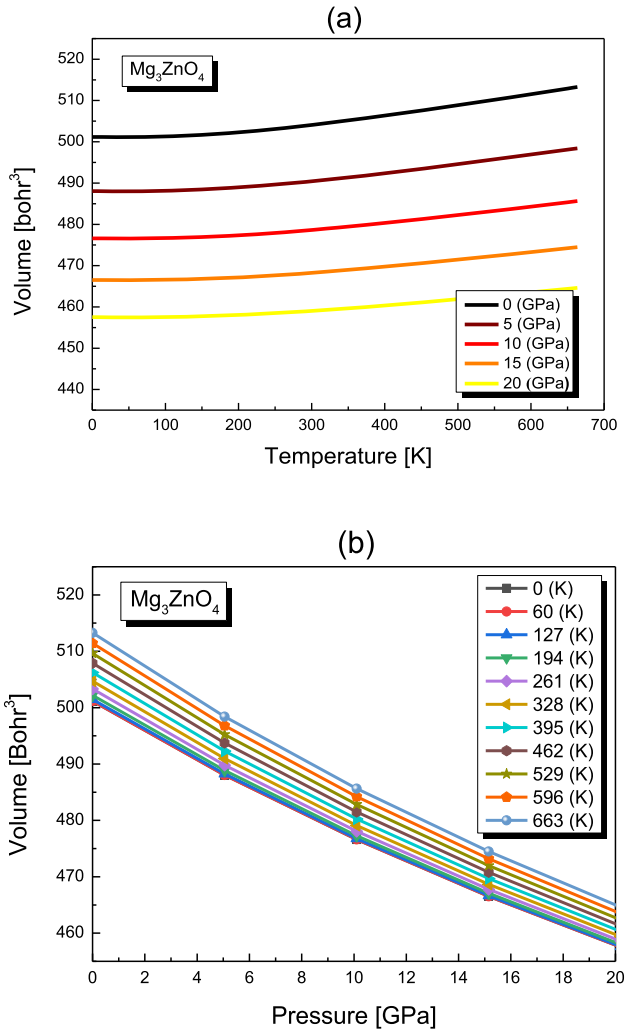

Fig. 16 Variation of the unit cell volume as a function of **a** temperature and **b** pressure for Mg3ZnO4 using LDA approximation

3.5.2 Effect of the V variation as a function of T and P

The variation of the unit cell volume for Mg_3ZnO_4 as a function of temperature and pressure, based on the Local Density Approximation (LDA), is depicted in Fig. 16. In Fig. 16a, it is evident that the unit cell volume exhibits a slight increase with rising temperature at a constant pressure. This thermal expansion is indicative of the material's response to increased atomic vibrations and lattice spacing as temperature increases.

Conversely, Fig. 16b illustrates the effect of pressure on the unit cell volume. As pressure is applied, the volume decreases, demonstrating the material's tendency to contract under compressive forces. This behavior reflects the lattice's response to increased external pressure, which effectively reduces the interatomic distances and, thus, the overall unit cell volume.

The interplay between temperature and pressure results in a diminishing rate of volume increase with rising temperature as pressure is increased. While temperature generally promotes expansion due to enhanced vibrational motion, pressure acts to counteract this effect by compressing the lattice structure.

For Mg_3ZnO_4, the calculated unit cell volume at 300 K and 0 GPa is 504.12 $Bohr^3$ (see Table 9). This value serves as a benchmark for understanding how thermal and compressive stresses influence the material's structural dimensions and provides a basis for evaluating its behavior under varying environmental conditions.

3.5.3 Effect of the BT variation as a function of T and P

The bulk modulus is a critical material property that quantifies a substance's resistance to volumetric deformation under applied pressure. In other terms, the bulk modulus (B) is defined as a measure of the pressure required to cause a unit change in volume [60]. It is a key indicator of how a material responds to compressive forces, providing insights into its mechanical stability and structural integrity.

Figure 17 illustrates the variation of the bulk modulus for Mg_3ZnO_4 as a function of temperature and pressure, calculated using the Local Density Approximation (LDA). As depicted in Fig. 17a, the bulk modulus decreases significantly with increasing temperature. This trend reflects the material's reduced resistance to compression at higher temperatures, which can be attributed to the enhanced atomic vibrations and increased lattice spacing that facilitate volumetric expansion.

Conversely, the effect of pressure on the bulk modulus, shown in Fig. 17b, indicates a near-linear increase in the bulk modulus with rising pressure across all studied temperatures. This behavior demonstrates that higher pressures enhance the material's resistance to volumetric changes, as the atomic or molecular interactions are compressed, leading to a more rigid lattice structure.

For Mg_3ZnO_4 at a standard condition of 300 K and 0 GPa, the calculated bulk modulus is 172.67 GPa (see Table 9). This value provides a reference for understanding the material's compressive properties and highlights the influence of temperature and pressure on its mechanical behavior. The bulk modulus serves as an important parameter for applications requiring materials with specific mechanical stability under varying environmental conditions.

3.5.4 Effect of the Cv variation as a function of T and P

The heat capacity (C) is the amount of heat required to change the temperature of one unit mass of a material by one degree, making it a fundamental property for describing the thermodynamic and thermophysical behaviors of a material system [97]. Specifically, the heat capacity at constant volume (Cv) of Mg_3ZnO_4, as a function of temperature and pressure, is depicted in Fig. 18. At low temperatures, Cv increases rapidly, reflecting the growing number of accessible vibrational

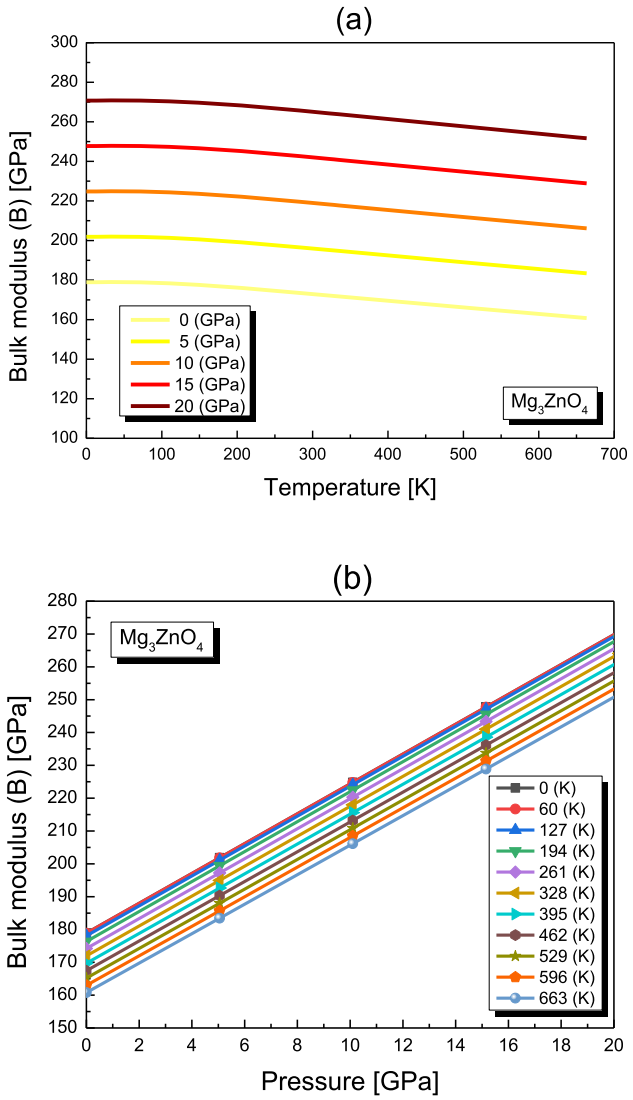

Fig. 17 Variation of the bulk modulus as a function of **a** temperature and **b** pressure for Mg3ZnO4 using LDA approximation

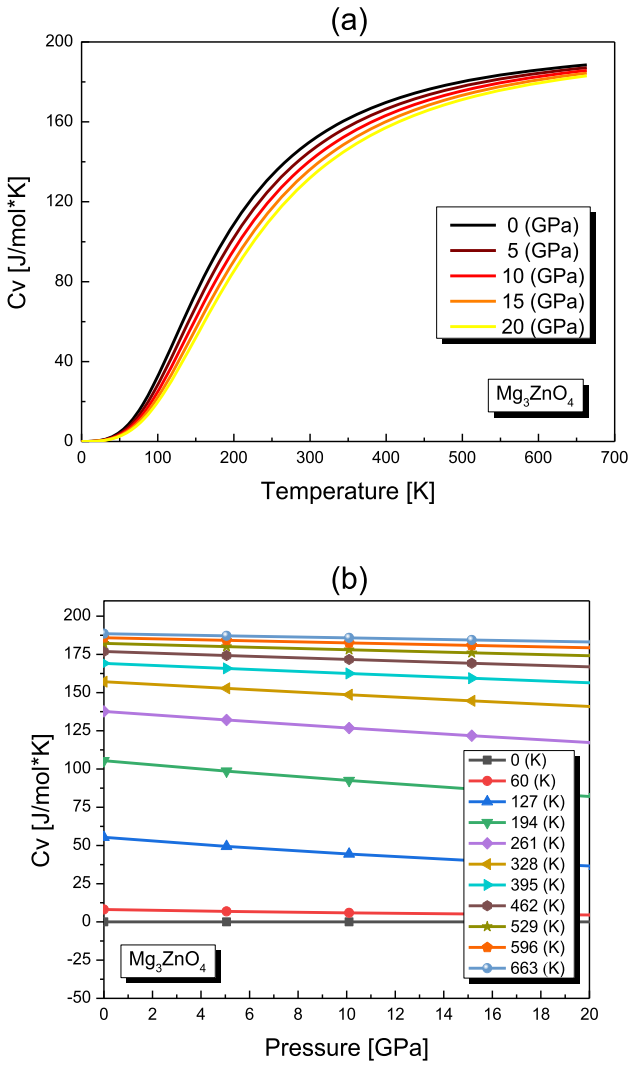

Fig. 18 Variation of specific heat capacity at constant volume (Cv) as a function of **a** temperature and **b** pressure for Mg_3ZnO_4 using LDA approximation

modes as thermal energy is added. This initial steep rise is typical of materials where low-energy vibrational modes are excited first. As the temperature continues to rise, the rate of increase in Cv slows down. At higher temperatures, Cv approaches the classical limit predicted by Dulong and Petit [98], where the heat capacity becomes nearly constant, reflecting the saturation of available vibrational modes.

The effect of pressure on Cv is also noteworthy. At a constant temperature, Cv decreases approximately linearly with increasing pressure. This trend indicates that higher pressure restricts the material's ability to absorb heat, due to the reduced vibrational amplitudes

Table 9 Thermal parameters at (T = 300 K): unit cell volume (V), bulk modulus B, specific heat capacities at stable volume (Cv) and at stable pressure (Cp), entropy (S), thermal expansion coefficient (α), and Debye temperature (θ_D) for Mg_3ZnO_4 within LDA approximation

Mg_3ZnO_4	T [K]	V [Bohr^3]	B_T [GPa]	Cv [J/mol*K]	Cp [J/mol*K]	S [J/mol*K]	α [10^{-5}/K]	θ_D [K]
Present results (LDA)	300	504.12	172.67	154.73	154.17	114.01	4.134	737.91

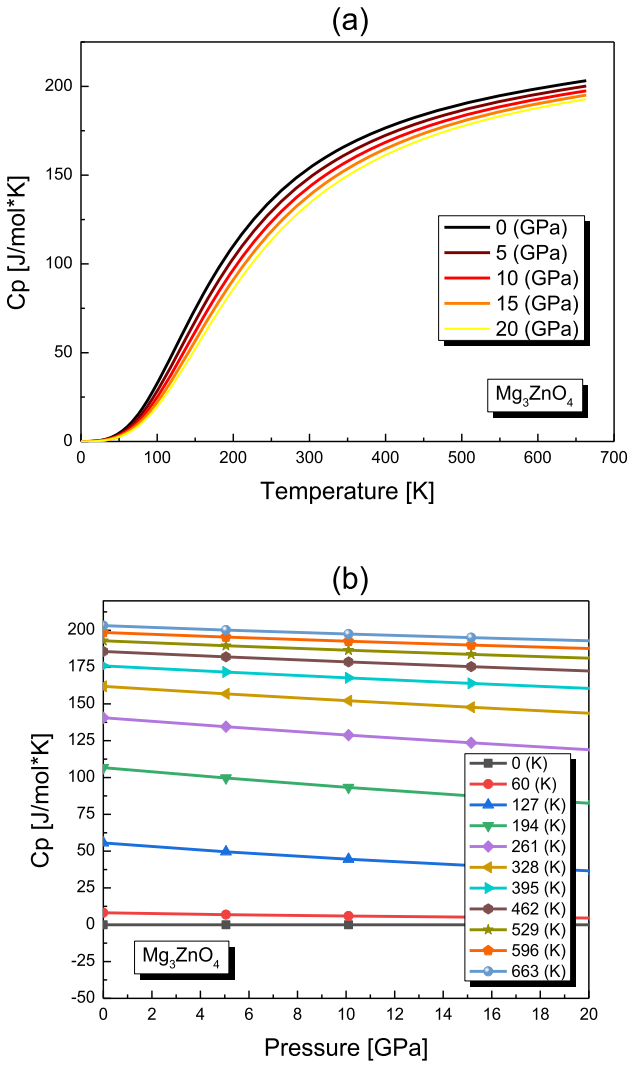

Fig. 19 Variation of specific heat capacity at constant pressure (Cp) as a function of **a** temperature and **b** pressure for Mg_3ZnO_4 using LDA approximation

and the constrained lattice structure. For Mg_3ZnO_4 at 300 K and 0 GPa, the calculated heat capacity at constant volume is 154.73 J/mol*K (see Table 9). This value offers a benchmark for understanding the material's thermal characteristics and highlights the interplay between temperature, pressure, and vibrational behavior.

3.5.5 Effect of the Cp variation as a function of T and P

The heat capacity at constant pressure (Cp) of Mg_3ZnO_4 as a function of temperature is depicted in Fig. 19. The analysis reveals distinct patterns in Cp behavior across different temperature ranges. At lower temperatures, the variation of Cp mirrors that of the heat capacity at constant volume (Cv), reflecting similar trends in how thermal energy is absorbed by the material.

As temperature increases, Cp shows a notable rise, particularly in the high-temperature range. This increase indicates that the material's capacity to absorb heat grows with temperature, a common characteristic resulting from the higher energy required to excite additional vibrational modes of the atoms within the lattice. Furthermore, the impact of pressure on Cp is also evident. At a constant temperature, Cp decreases with increasing pressure, demonstrating that higher pressure conditions limit the material's ability to absorb heat. This decrease in Cp with pressure is almost linear, suggesting a direct relationship between pressure and the material's thermal capacity.

At standard conditions of 300 K and 0 GPa, the calculated heat capacity at constant pressure for Mg_3ZnO_4 is 154.17 (J/mol*K) (see Table 9). This value provides essential information about the material's thermal properties and its response to changes in temperature and pressure. Understanding these characteristics is crucial for applications that involve thermal management and material performance under varying conditions.

3.5.6 Effect of the entropy (S) variation as a function of T and P

Entropy denoted by S is a fundamental thermodynamic property that quantifies the degree of randomness or disorder of energy within a system, such as the distribution of energy among atoms or molecules. As entropy increases, energy spreads more evenly, making the system less structured. It varies with the amount of matter present and reflects the degree of order within a thermodynamic system [99].

Figure 20 presents the calculated entropy of Mg_3ZnO_4 as a function of temperature, with calculations taken at various pressures. The data reveal a nearly linear increase in entropy with rising temperature, indicating that the disorder within the material grows as thermal energy is added. This trend reflects the increasing number of accessible microstates and the greater randomness in the material's atomic or molecular arrangement as temperature increases.

Conversely, the entropy values decrease with increasing pressure at a given temperature. This behavior suggests that higher pressure tends to reduce the degree of disorder in the material due to the compression of atomic or molecular distances, which limits the system's capacity to explore various microstates.

At standard conditions of 300 K and 0 GPa, the calculated entropy for Mg_3ZnO_4 is 114.01 J/mol*K (see Table 9). This value provides a baseline for understanding the material's thermodynamic properties and offers a reference for assessing how entropy evolves with temperature and pressure. The observed trends in entropy are critical for predicting the material's stability and behavior under different thermodynamic conditions, influencing its suitability for various applications.

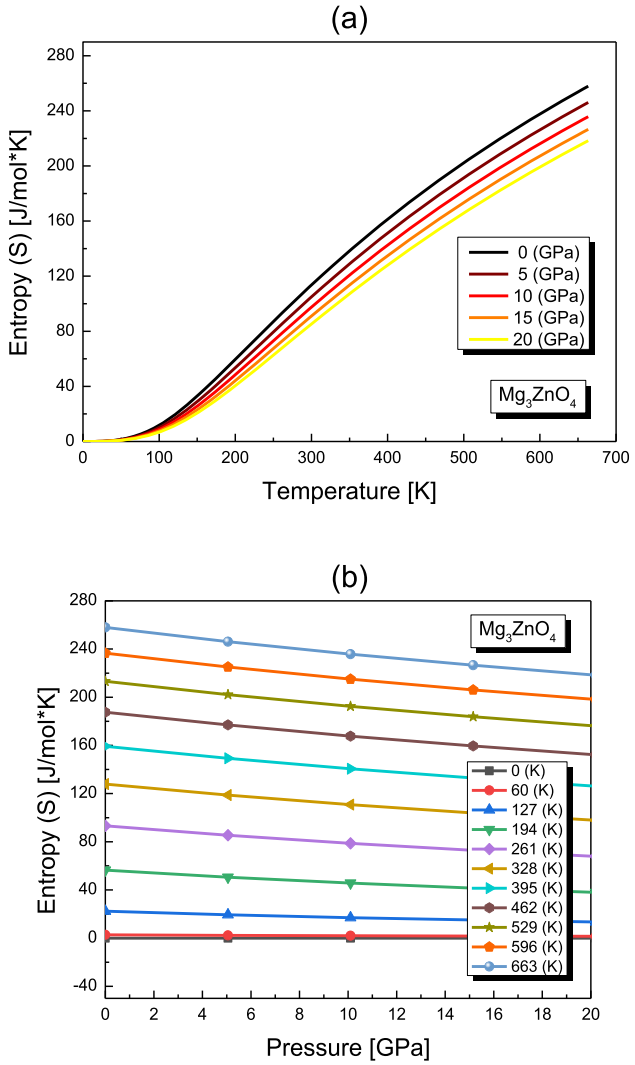

Fig. 20 Variation of entropy (S) as a function of **a** temperature and **b** pressure for Mg3ZnO4 using LDA approximation

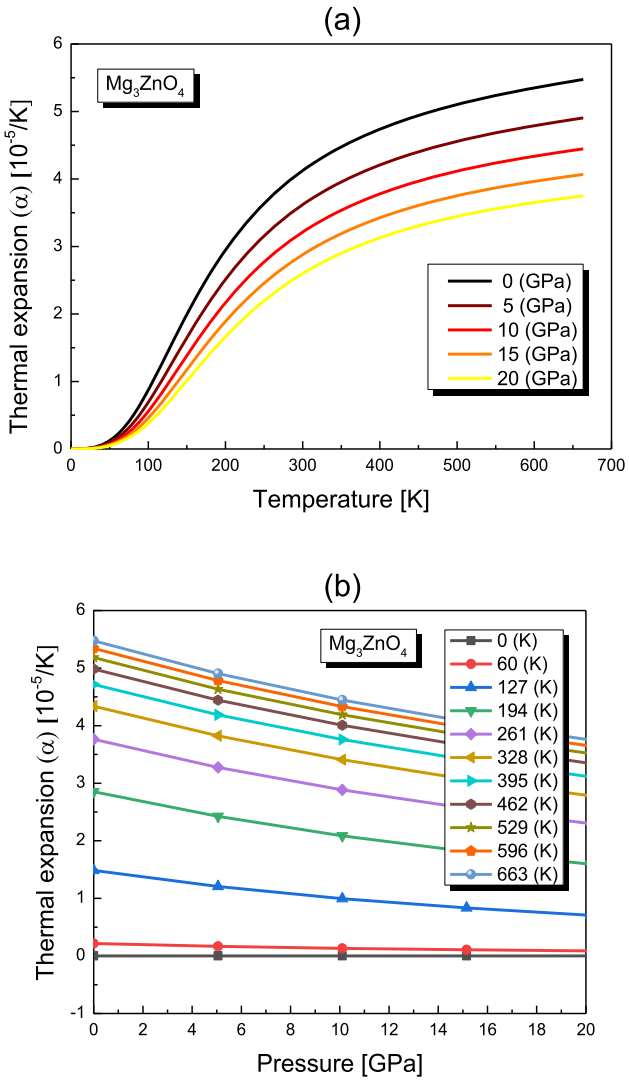

Fig. 21 Variation of thermal expansion as a function of **a** temperature and **b** pressure for Mg3ZnO4 using LDA approximation

3.5.7 Effect of the thermal expansion (α) variation as a function of T and P

The thermal expansion coefficient is an important thermodynamic parameter that express the volume change of a substance due to temperature change [100]. This coefficient is essential for understanding the material's thermal behavior, especially in applications where temperature fluctuations are significant. Figure 21 illustrates the variation of the thermal expansion coefficient of Mg_3ZnO_4 as a function of temperature, calculated at different pressures. The data reveal that, at constant pressure, the thermal expansion coefficient increases markedly with temperature up to 400 K. This sharp rise indicates that the material's volume expands significantly with increasing temperature in this range. However, beyond 400 K, the rate of increase in the thermal expansion coefficient slows down, and the relationship between temperature and thermal expansion becomes nearly linear. This suggests that at higher temperatures, the material's volume expansion rate levels off, and temperature changes exert a diminishing effect on thermal expansion. Additionally, the sensitivity of thermal expansion to pressure changes is evident from the data. At atmospheric pressure ($P = 0$ GPa), the thermal expansion coefficient is notably higher, reflecting the material's greater volume expansion in response to temperature increases. Conversely, at higher pressures, the thermal expansion coefficient decreases, indicating that applied pressure inhibits the material's volumetric expansion. This effect underscores the influence of pressure on constraining the material's thermal response. At standard conditions of 300 K and 0 GPa, the thermal expansion coefficient for Mg_3ZnO_4 is calculated to be 4.134 (10^{-5}/K) (see Table 9). This value provides a

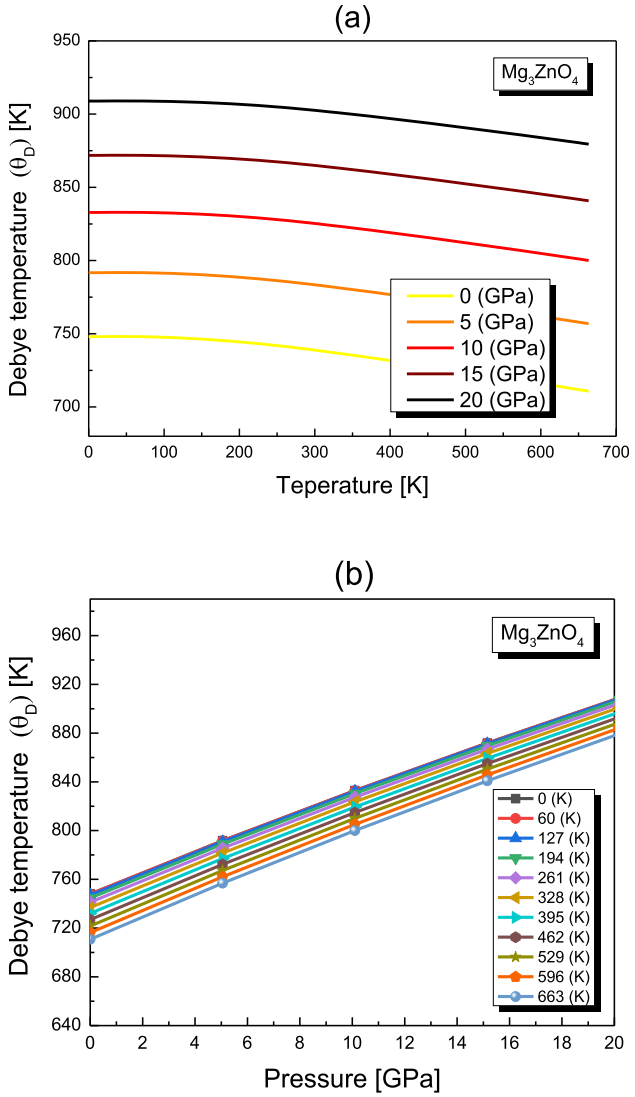

Fig. 22 Variation of Debye temperature (θ_D) as a function of **a** temperature and **b** pressure for Mg3ZnO4 using LDA approximation

benchmark for understanding how the material's volume changes with temperature and highlights its thermal stability and behavior under different pressure conditions.

3.5.8 Effect of Debye temperature (θ_D) variation as a function of T and P

The Debye temperature (θ_D) is a fundamental thermal property that provides insight into various physical characteristics of a material, including its elastic constants, specific heat, and melting temperature [101]. This property is crucial for understanding the thermal behavior of materials, as it reflects the highest temperature at which specific heat capacity approaches the Dulong–Petit [98] limit.

As illustrated in Fig. 22a, the Debye temperature for Mg_3ZnO_4 exhibits a relatively stable value from 0 to 200 K, indicating minimal temperature dependence in this range. However, a notable trend is observed beyond 250 K, where θ_D decreases linearly with increasing temperature. This decline is indicative of the temperature-induced changes in the vibrational modes of the lattice, which impact the material's heat capacity and overall thermal behavior.

Additionally, the effect of pressure on the Debye temperature is significant. Figure 22b demonstrates that θ_D increases linearly with applied pressure, reflecting the enhancement of lattice vibrations under compressive forces. Conversely, at a constant pressure, θ_D shows a decreasing trend with rising temperature. This behavior suggests that while higher pressure tends to stabilize and increase the vibrational frequencies of the lattice, higher temperatures lead to a broader distribution of vibrational modes, thereby reducing θ_D. At standard conditions (300 K and 0 GPa), the Debye temperature for Mg_3ZnO_4 is calculated to be 737.91 K (refer to Table 9). This value provides a baseline for understanding the material's thermal properties and its response to temperature and pressure variations. The observed trends in θ_D highlight the interplay between thermal and mechanical factors in influencing the vibrational characteristics of the material, offering valuable insights for applications that require precise thermal management and stability.

4 Conclusion

This comprehensive investigation into the structural, electronic, optical, elastic, and thermodynamic properties of the cubic mixed metal oxide Mg_3ZnO_4 in its rocksalt phase has yielded significant insights into its fundamental characteristics, demonstrating its remarkable potential for various advanced applications in optoelectronics and beyond. The structural analysis confirms that Mg_3ZnO_4 crystallizes in a cubic $Pm\bar{3}m$ space group**,** adopting a crystallographic structure akin to the mineral Caswellsilverite. The optimized lattice parameters and refined atomic arrangement underscore the inherent stability and high symmetry of the crystal structure. This foundational understanding is crucial for predicting the material's behavior under diverse conditions and applications, providing a robust basis for further theoretical and experimental explorations. Notably, the calculated formation energy confirms the stability of the rocksalt structure, enhancing its suitability for optoelectronic devices, particularly in applications where structural integrity is paramount. Key findings also reveal that Mg_3ZnO_4 offers high mechanical strength alongside a UV-located band gap**,** establishing it as a formidable candidate for a wide range of optoelectronic devices. The electronic structure calculations reveal a well-defined energy band gap situated within the ultraviolet range, indicative of its semiconducting nature. This band gap not only influences

the material's electronic conductivity but also determines its interaction with light and external electrical stimuli, thereby shaping its overall electronic transport properties. The presence of this wide band gap suggests that Mg_3ZnO_4 is particularly well suited for applications in UV detectors and high-efficiency photovoltaic cells, where precise control over electronic behavior is paramount. Thorough investigations of the optical properties elucidate that Mg_3ZnO_4 is transparent in the visible spectrum**,** exhibiting efficient light absorption and energy transfer mechanisms. The calculations of the dielectric function indicate that the material has high reflectivity and a tailored refractive index, making it ideal for use in organic/inorganic photovoltaic solar cells and UV light-emitting diodes (LEDs). Such optical characteristics are critical for enhancing the performance and efficiency of these devices. Additionally, the elastic properties of Mg_3ZnO_4, including Young's modulus, shear modulus, and Poisson's ratio, offer a comprehensive understanding of its mechanical strength and ductility. This material's ability to withstand significant mechanical stress without failure underscores its robustness, making it suitable for applications in flexible electronics and protective coatings where resilience is vital.

The thermodynamic analysis reveals how Mg_3ZnO_4 responds to changes in temperature, pressure, and energy, essential for predicting its behavior under varying environmental conditions. The material's favorable thermal stability and conductivity position it as a strong candidate for heat management applications, such as in thermoelectric devices and temperature-sensitive sensors, where effective thermal management is crucial. Collectively, these findings underscore the viability of Mg_3ZnO_4 for advanced optoelectronic applications, highlighting its unique combination of structural integrity, favorable electronic behavior, and efficient optical response. The integration of high mechanical strength, a UV-located band gap, and transparency in the visible range makes Mg_3ZnO_4 a promising material for the development of high-performance organic/inorganic photovoltaic solar cells, UV photodetectors, LEDs, and other devices where optical and electronic performance are critical. The insights gained from this study pave the way for future research and development to harness the full potential of Mg_3ZnO_4's properties for innovative technological applications. Future studies may explore doping strategies to further tailor its electronic and optical properties, investigate its behavior under different environmental conditions, and experimentally validate the predicted properties to confirm its viability for large-scale production and deployment in commercial devices. By leveraging the unique characteristics of Mg_3ZnO_4, we can potentially drive advancements in optoelectronic technologies and expand the boundaries of material science in practical applications.

Acknowledgements Authors from Algeria are grateful to the General Directorate for Scientific Research and Technological Development (DGRSDT) of Algeria. This work falls under the PRFU research Project No. A10N01UN280120220006. O. Guskova acknowledges Deutsche Physikalische Gesellschaft (Project GU1510/3-1).

Author contributions

M. Hadjab: conceptualization, formal analysis, methodology, writing—review and editing, software, and investigation. M-I. Ziane: formal analysis, and writing—review and editing, visualization. A. Hadj Larbi: data curation, and writing—review and editing. H. Bennacer: data curation and writing. M. Faraji: data curation and writing—review and editing. O. Guskova: writing—review and editing.

Data availability statement The data that support the findings of this study are available from the corresponding author, M. Hadjab, upon reasonable request.

References

1. Y. Pan, M. Wen, J. Am. Ceram. Soc. **107**, 1081–1089 (2024)
2. Y. Pan, J. Phys. Chem. Solids **174**, 111152 (2023)
3. M. Mishra, R. Saha, L. Tyagi et al., J. Lumin. **257**, 119748 (2023)
4. C.L. Heng, X.L. Li, X. Wang et al., J. Alloy. Compd. **981**, 173704 (2024)
5. D. Thapa, J. Huso, K. Miklos et al., J. Mater. Sci.: Mater. Electron. **28**, 2511–2520 (2017)
6. C.X. Shan, J.S. Liu, Y.J. Lu, B.H. Li, F.C.C. Ling, D.Z. Shen, Opt. Lett. **40**, 3041–3044 (2015)
7. S. Boudour, I. Bouchama, N. Bouarissa et al., J. Sci. Adv. Mater. Dev. **4**, 111–115 (2019)
8. M. Hadjab, J.-M. Wagner, F. Bouzid et al., Int. J. Model. Simul. **42**(2), 179–191 (2022)
9. S.-D. Baek, D.-K. Kwon, Y.C. Kim et al., ASC Appl. Mater. Interfaces **12**, 6037–6047 (2020)
10. Y. Li, F. Yu, G. Li et al., Phys. Status Solidi A **219**, 2200313 (2022)
11. C. Li, Z. Zhang, H. Chen et al., Thin. Solid Films **548**, 456–459 (2013)
12. H.-J. Lee, J.-W. Kang, S.-H. Hong et al., ASC Appl. Mater. Interfaces **8**(3), 1565–1570 (2016)
13. S. Han, D. Yue, P. Cao et al., Opt. Mater. **147**, 114612 (2024)
14. B. Amrani, R. Ahmed, F. El-Haj-Hassan, Comput. Mater. Sci. **40**(1), 66–72 (2007)
15. F.Z. Aoumeur-Benkabou, M. Ameri, A. Kadoun et al., Model. Numer. Simul. Mater. Sci. **2**(3), 60–66 (2012)
16. S.Y. Savrasov, D.Y. Savrasov, Phys. Rev. B **46**(19), 12181–12195 (1992)
17. J.P. Perdew, Y. Wang, Phys. Rev. B **45**(13), 13244–13249 (1992)
18. J.P. Perdew, S. Burke, M. Ernzerhof, Phys. Rev. Lett. **77**, 3865 (1996)
19. E. Engel, S.H. Vosko, Phys. Rev. B **47**, 13164 (1993)
20. N. Drissi, A. Gueddim, N. Bouarissa, Philos. Mag. **100**(12), 1620–1635 (2020)

21. M. Hadjab, S. Berrah, H. Abid et al., Mater. Chem. Phys. **182**, 182–189 (2016)
22. Z. Wu, R.E. Cohen, Phys. Rev. B **73**, 235116 (2006)
23. F. Tran, P. Blaha, Phys. Rev. Lett. **102**, 226401 (2009)
24. A. Ohtomo, M. Kawasaki, T. Koida et al., Appl. Phys. Lett. **72**, 2466 (1998)
25. Y.W. Heo, L.C. Tien, D.P. Norton, J. Mater. Res. **20**, 3028 (2005)
26. J.H. Kim, B. Kim, D. Andeen et al., J. Mater. Res. **22**, 943 (2007)
27. X. Chen, J. Kang, Semicond. Sci. Technol. **23**, 025008 (2008)
28. S. Chen, N. Wang, Y. Wang et al., Appl. Surf. Sci. **653**, 159439 (2024)
29. F. Tian, D. Duan, D. Li et al., Sci. Rep. **4**, 5759 (2014)
30. K. Kaneko, T. Onuma, K. Tsumura et al., Appl. Phys. Express **9**, 111102 (2016)
31. P. Dłużewski, J.Z. Domagala, S. Kret et al., J. Chem. Phys. **154**, 154701 (2021)
32. A. Zaoui, M. Ferhat, Superlatt. Microstruct. **145**, 106623 (2020)
33. www.materialsproject.org (Last access 15.06.2024).
34. P. Giannozzi, S. Baroni, N. Bonini et al., J. Phys. Conden. Matter **21**, 395502 (2009)
35. Y. Pan, Z. Yang, H. Zhang, Diam. Relat. Mater. **144**, 110966 (2024)
36. P. Blaha, K. Schwarz, G.H. Madsen et al., *WIEN2k: an augmented plane wave plus local orbitals program for calculating crystal properties* (Vienna University of Technology, Austria, 2018)
37. P. Blaha, K. Schwarz, F. Tran, J. Chem. Phys. **152**, 074101 (2020)
38. P. Hohenberg, W. Kohn, Phys. Rev. B **136**, 864–871 (1964)
39. W. Kohn, L.J. Sham, Phys. Rev. A **140**, 1133–1138 (1965)
40. Data retrieved from the Materials Project for Mg_3ZnO_4 (mp–1024045) from database version v2023.11.1.
41. J.P. Perdew, A. Ruzsinszky, G.I. Csonka et al., Phys. Rev. Lett. **100**, 136406 (2008)
42. M. Hadjab, O. Guskova, H. Bennacer et al., Mater. Today Commun. **32**, 103995 (2022)
43. A.D. Becke, M.R. Roussel, Phys. Rev. A **39**, 3761 (1989)
44. M. Hadjab, S. Berrah, H. Abid et al., Optik **127**, 9280–9249 (2016)
45. F.D. Murnaghan, Proc. Natl. Acad. Sci. USA **30**, 244–247 (1944)
46. H. Serai, M.I. Ziane, H. Bennacer et al., Optik **306**, 171794 (2024)
47. A. Delin, Opt. Commun. **167**, 105–109 (1999)
48. J. Zhu, Y. Pan, Mater. Sci. Eng. B **308**, 117554 (2024)
49. Y. Pan, Z. Yang, H. Zhang, Int. J. Hydrogen Energy **82**, 1308–1313 (2024)
50. Y. Pan, F. Yang, J. Energy Storage **87**, 111492 (2024)
51. M.E.A. Miloudi, Y. Liu, Y. Ge et al., Surf. Interfaces **27**, 101545 (2021)
52. O. Ouadah, F. Saidi, M.E.A. Miloudi et al., Int. J. Hydrogen Energy **46**, 32962–32973 (2021)
53. M. Hadjab, M. Ibrir, S. Berrah et al., Optik **169**, 69–76 (2018)
54. A.H. Larbi, S. Hiadsi, M. Hadjab et al., Optik **166**, 169–176 (2018)
55. M.I. Ziane, M. Tablaoui, A. Khelfane et al., Optik **157**, 248–258 (2018)
56. M.I. Ziane, H. Bennacer, M. Mostefaoui et al., Optik **243**, 167490 (2021)
57. H. Bennacer, A. Boukortt, S. Meskine et al., Optik **159**, 229–244 (2018)
58. X. Ma, D. Li, S. Zhao et al., Nanoscale Res. Lett. **9**(580), 1–8 (2014)
59. Q.-J. Liu, Z.-T. Liu, J.-C. Chen et al., Phys. B **406**, 3377–3382 (2011)
60. A. Candan, J. Electron. Mater. **48**(12), 7608–7622 (2019)
61. L.D. Landau, E.M. Lifshitz, *Theory of elasticity*, 3rd edn. (Pergamon Press, Oxford, 1986)
62. J.F. Nye, *Physical properties of crystals: their representation by tensors and matrices* (Oxford University Press, Oxford, 1985)
63. M. Born, Math. Proc. Camb. Philos. Soc. **36**, 160–172 (1940)
64. M. Born, K. Huang, *Dynamics theory of crystal lattices* (Oxford University Press, Oxford, 1954)
65. Y. Pan, Inorg. Chem. **63**, 8264–8272 (2024)
66. S.F. Pugh, Lond. Edinb. Dublin Philos. Mag. J. Sci. **45**(367), 823–843 (1954)
67. W. Voigt, *Lehrbuch der Kristallphysik*, 2nd edn. (LeipzigTeubner Verlag, Berlin, 1928)
68. A. Reuss, ZAMM-J. Appl. Math. Mech. Zeitschrift für Angewandte Mathematik und Mechanik **9**, 49–58 (1929)
69. R. Hill, J. Mech. Phys. Solids **11**, 357–372 (1963)
70. E. Schreiber, O.L. Anderson, N. Soga, *Elastic constants and their measurements*, 1st edn. (McGraw-Hill, New York, 1974)
71. R. Hill, Proc. Phys. Soc. Sect. A **65**, 349–354 (1952)
72. M.E.A. Miloudi, Y. Liu, Y. Ge et al., Mater. Sci. Semicond. Process. **145**, 106649 (2022)
73. M.E.A. Miloudi, Y. Liu, Y. Ge et al., J. Phys. Chem. Solids **170**, 110902 (2022)
74. O. Ouadah, M. Benaissa, M.E.A. Miloudi et al., J. Solid State Chem. **309**, 122952 (2022)
75. Y. Pan, J. Zhu, Mater. Today Commun. **38**, 108428 (2024)
76. Y. Pan, F. Yang, Ceram. Int. **50**, 14856–14864 (2024)
77. I. N. Frantsevich, F. F. Voronov, S. A. Bokuta (1983) Elastic constants and elastic moduli of metals and insulators handbook. In: I.N. Frantsevich (Ed) Naukova Dumka, Kiev, pp. 60–180
78. Md.A. Rahman, K. Mousumi, Md.L. Ali et al., Results Phys. **44**, 106141 (2023)
79. J. Haines, J.M. Leger, G. Bocquillon, Annu. Rev. Mater. Res. **31**, 1–46 (2001)
80. Z.T.Y. Liu, D. Gall, S.V. Khare, Phys. Rev. B **90**, 134102 (2014)
81. Y. Tian, B. Xo, Z. Zhai, Int. J. Refract Metal Hard Mater. **33**, 93–106 (2012)
82. S.I. Ranganathan, M. Ostoja-Starzewski, Phys. Rev. Letter **101**, 055504 (2008)
83. P. Ravindran, L. Fast, P.A. Korzhavyi et al., J. Appl. Phys. **84**, 4891–4904 (1998)
84. S. Kumar, J.P. Jung, Mater. Sci. Eng. B **178**, 10–21 (2013)

85. B. Huang, Y.H. Duan, W.C. Hu et al., Ceram. Int. **41**, 6831–6843 (2015)
86. O. Gomis, F.-J. Manjón, P. Rodríguez-Hernández et al., J. Phys. Chem. Solids **124**, 111–120 (2019)
87. Q. Wu, S. Li, Comput. Mater. Sci. **53**, 436–443 (2012)
88. J.M. Zhang, Y. Zhang, K.W. Xu et al., J. Phys. Chem. Solids **68**(4), 503–510 (2007)
89. O.L. Anderson, J. Phys. Chem. Solids **24**, 909–917 (1963)
90. Y. Pan, Int. J. Refract Metal Hard Mater. **121**, 106676 (2024)
91. N. W. Ashcroft, N. D. Mermin, "Solid State Physics" Harcourt College Publishers (1976)
92. A. Otero-de-la-Roza, D. Abbasi-Perez, V. Luana, Comput. Phys. Commun. **182**, 2232 (2011)
93. M.A. Blanco, A.M. Pendás, E. Francisco et al., J. Mol. Struct. Theochem **368**, 245–255 (1996)
94. C. Dong, C. Jing-Dong, Z. Li-Hua et al., Chin. Phys. B **18**(2), 738–743 (2009)
95. K. Kalaliz, A. Chahed, M.A. Boukli et al., Revista Mexicana de Física **67**(6), 060501 (2021)
96. M.A. Blanco, E. Francisco, V. Luaña, Comput. Phys. Commun. **158**(1), 57–72 (2004)
97. R. Bhowmik, S. Sihn, V. Varshney et al., Polymer **167**, 176–181 (2019)
98. P.L. Dulong, A.T. Petit, Annales de Chimie et de Physique **10**, 395–413 (1819)
99. Md.Z. Rana, Md.R. Munshi, Md. Al Masud et al., Heliyon **9**, e21405 (2023)
100. L. Dubrovinsky, Encyclop. Mater. Sci. Technol., 1–4
101. W.H. Lee, X.H. Yao, Comput. Mater. Sci. **106**, 76–82 (2015)